

Advanced 3D Monte Carlo algorithms for bio-photonic and medical applications

Lewis McMillan



University of
St Andrews

This thesis is submitted in partial fulfilment for the degree of
PhD
at the
University of St Andrews

March 2019

Contents

Abbreviations	v
List of Figures	viii
1 Monte Carlo radiation transport technique	1
1.1 Introduction and Background	1
1.1.1 Monte Carlo method	1
1.2 Monte Carlo radiation transport algorithm	3
1.2.1 Introduction & background	3
1.2.1.1 Radiative transfer	3
1.2.2 MCRT algorithm	7
1.2.2.1 Grid set-up	7
1.2.2.2 Photon launch	7
1.2.2.3 Photon move	8
1.2.2.4 Photon scatter and absorbing	9
1.2.2.5 Termination	9
1.2.3 Code details	9
1.3 Validation of MCRT code	9
1.4 Optical properties	9
1.4.1 Scattering	10
1.4.2 Anisotropy	10
1.4.3 Absorption	11
1.4.4 Refractive index	12
1.4.5 Other parameters	12
1.5 Further extensions to the code	12
1.5.1 Fresnel reflections & refractions	12
1.5.2 Parallelisation of the Monte Carlo radiation Transfer (MCRT) algorithm	12
1.6 Improving the voxel tissue model	12
2 Computational modelling of tissue ablation	15
2.1 Introduction and background	15
2.2 Methods	16
2.2.1 Monte Carlo radiation transport (MCRT)	16
2.2.2 Heat transport	19
2.2.3 Tissue Damage	23
2.2.3.1 Introduction	23
2.2.3.2 Modelling coagulation damage	27
2.2.3.3 Modelling physical tissue damage	27

2.2.4	Validation	28
2.2.4.1	Heat transport validation	28
2.2.4.2	MCRT & heat transport validation	29
2.3	<i>In silico</i> results	30
2.3.1	Introduction	30
2.3.1.1	Optical & thermal properties	31
2.3.1.2	Computational speed up:	32
2.3.2	Results	33
2.3.2.1	Investigating ablation temperature, T_a	33
2.3.2.2	Investigating Thermal damage	34
2.4	Conclusion	34
	Appendix A Heat equation derivation	41

Abbreviations

T_a ablation temperature.

AMR adaptive mesh refinement.

FDM finite difference method.

K-M theory Kubelka-Munk Theory.

MCRT Monte Carlo radiation Transfer.

MPI Message-passing interface.

OCT optical coherence tomography.

PDF probability density function.

PDT photo-dynamic therapy.

RTE radiative transfer equation.

List of Figures

1.1	Sample buffon needle experiment. 100 needles are dropped on a 10 by 10 cm area with lines spaced 1.5cm apart. If a needle lands on a line it is recorded and coloured blue, else it is yellow. This simulation gave a value of pi as 3.17.	2
1.2	Computer generated imagery using ray-tracing. Code usd to create image available at: https://github.com/lewisfish/RayTran	3
1.3	Energy flow through area dA within solid angle $d\Omega$ in a direction \hat{s} . Adapted from [16,17]	4
1.4	Cylindrical volume element, $ds \cdot dA$, with solid angle $d\Omega$ in direction \hat{s} and solid angle $d\Omega'$ in direction \hat{s}' . Energy flowing through this element is used to derive the radiative transfer equation (RTE). Adapted from [16,17].	6
1.5	Spectra of some of the more common absorbers found in the skin.	11
2.1	Example of a possible voxel model, with three different layers, various holes due to ablative pixel beam lasers. Each voxel can represent a different optical/thermal property of the tissue medium.	17
2.2	Flowchart of the tissue ablation algorithm.	18
2.3	Red lines are photon paths within a voxel. Black lines photon paths out with the voxel. Red photon paths, weighted by μ_a , are summed up in order to calculate the absorbed energy within each voxel.	18
2.4	Discretisation of $f(x)$.	20
2.5	Finite difference method stencil for simple explicit scheme	21
2.6	Computational domain decomposition. Total computational domain (red outline) is evenly divided between cores in the CPU. This is done via layers of the domain in the z direction. Information is passed to/from cores via the ‘halo swap’ process (see Fig. 2.7).	24
2.7	Halo swapping. Process A updates the area in red and blue on the left. It updates the blue area which is sent to process B as B’s ‘halo’. Process B cannot update its own halo, but rather updates the halo for process A.	25
2.8	Tissue ablations, as viewed under a microscope. Steam vacuoles are clearly visible either side of the ablation area. Carbonisation is also evident at the edges of the ablation fronts. Adapted from [54].	26
2.9	Comparison between analytical solution and numerical method at $t=0.1$ s.	30
2.10	Water absorption coefficient for wavelengths 0-12000nm [72]. Data shows that water is highly absorbing in the infra-red portion of the spectrum compared to the visible portion.	31
2.11	Simulation of 81 pixel beams. Figure is a slice through the optical properties at the end of the simulation. Yellow is unchanged tissue, and purple is completely ablated tissue. Figure shows that the ablation craters do not overlap one another.	32

2.12	Simulations of 30 W and 70 W CO ₂ ablative laser. Crater depths as a function of pixel beam energy for various ablation temperature (T_a)'s. *placeholder until I rerun for triangular pulse.*	33
2.13	Tissue thermal damage around the ablation crater (white). Thermal tissue damage values of 3 refer to 3 rd degree burns, 2 to 2 nd , and 1 to 1 st degree burns respectively. P is the power in Watts, T_a is the ablation temperature in Kelvin, and E_p is the energy per pixel beam in mJ.	35
2.14	Figure shows the maximum horizontal extent of thermal damage as a function of energy per pixel beam for laser of power 30 W.	36
2.15	Figure shows the maximum horizontal extent of thermal damage as a function of energy per pixel beam for laser of power 70 W.	37
2.16	Figure shows the extent of burns inflicted by the laser as a function of depth. Lines are taken from the central point of the laser beam through the tissue. Coloured dashed lines are 30W laser and solid coloured lines are 70W laser. Both data sets plotted for ablation temperature of 420 °C, and pixel beam energy of 400 mJ .	38

Chapter 1

Monte Carlo radiation transport technique

1.1 Introduction and Background

This chapter will provide an overview of the Monte Carlo method and how it is used within the context of MCRT. The chapter will then present the details of the MCRT code used as the basis of the subsequent chapters. Validation of this code and details of computational speed up are also presented. Subsequent chapters will expand upon the code for each individual projects needs.

1.1.1 Monte Carlo method

The Monte Carlo method is a numerical analysis technique based upon random numbers, which are used to calculate unknown variables in problems.

The earliest use of the method is in Buffon's needle experiment of the 18th century [1–3]. Buffon asked the question;

“Suppose we have a floor made of parallel strips of wood, each the same width, and we drop a needle onto the floor. What is the probability that the needle will lie across a line between two strips?”

The solution to this question is as: for a needle length l , strip separation s , and where x is the distance from the needle to the closest line. Then using a simple geometrical argument, a needle crosses a strip if $x \leq \frac{l}{2} \sin\theta$.

x is distributed uniformly in $[0, \frac{s}{2}]$, and θ in $[0, \frac{\pi}{2}]$. Therefore the probability density function for x is $p(x) = \frac{2}{s}$, and θ is $p(\theta) = \frac{2}{\pi}$. The **probability density function (PDF)**, is a function of a variable that gives probability for a variable to take a given value. The **PDF** is normalised over the whole range of the variable, in this case x , and θ . Thus, as x and θ are independent variables, giving a joint probability of $p(x, \theta) = \frac{4}{s\pi}$. So the probability of a needle of length l ($l < s$) is:

$$P = \int_0^{\frac{\pi}{2}} \int_0^{\frac{l}{2} \sin\theta} \frac{4}{s\pi} dx d\theta = \frac{2l}{s\pi} \quad (1.1)$$

Equation (1.1) can be used to carry out a Monte Carlo estimation of pi. A simple rearrangement yields: $\pi = \frac{2l}{sP}$ where P is the ratio of needles crossing the line over total number dropped.

Laplace was the first to suggest that Buffon's needle experiment could be used to estimate π [2]. Figure 1.1 shows an example of simulation of Buffon's needle experiment.

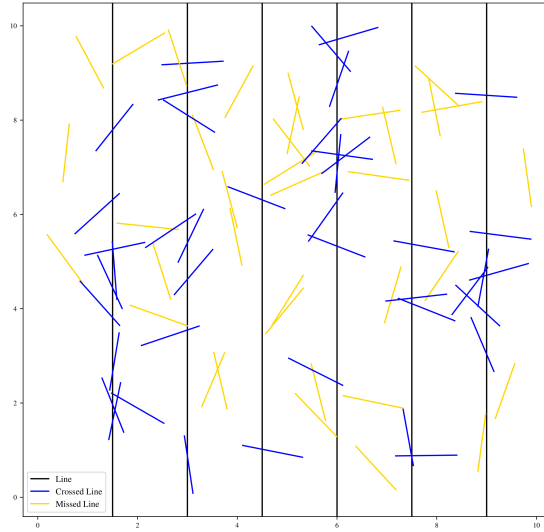


Figure 1.1: Sample buffon needle experiment. 100 needles are dropped on a 10 by 10 cm area with lines spaced 1.5cm apart. If a needle lands on a line it is recorded and coloured blue, else it is yellow. This simulation gave a value of pi as 3.17.

The Monte Carlo method is used in various different disciplines. Ranging from use in the financial sector to analyse investments and stocks by simulating the sources of uncertainty which affect their values [4,5], use in statistical analysis [6], and in modern computer generated images (see Fig. 1.2) [7,8]. It is also widely used in astronomy and medicine, in order to simulate the propagation of particles through turbid media. This technique, Monte Carlo radiation transfer, is what makes up the bulk of this thesis and is described in depth in the following sections.

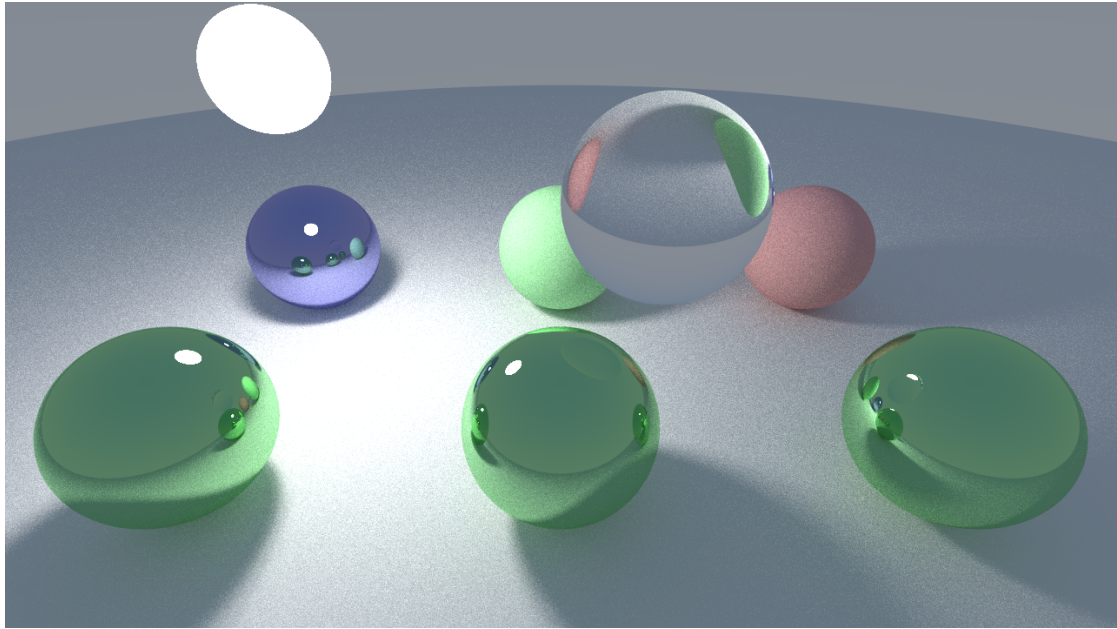


Figure 1.2: Computer generated imagery using ray-tracing. Code used to create image available at: <https://github.com/lewisfish/RayTran>

1.2 Monte Carlo radiation transport algorithm

1.2.1 Introduction & background

The technique that makes up the bulk of this thesis, is the [MCRT](#) technique. This method was developed at the tail end of the Second World War at the Los Alamos National Laboratory, for the purpose of calculating neutron diffusion through shielding material [9–12]. It has since found a myriad of applications from light transport through dusty clouds [13], calculating doses for radiotherapy [14] to light transport through tissue [15].***more here + link to next section***

1.2.1.1 Radiative transfer

Transport of photons through turbid media, can be modelled analytically using the [RTE](#). The [RTE](#) models the radiative losses, and gains by a beam of radiation as it travels through a medium, including: loss of energy due to absorption, loss/gain of energy due to scattering, and energy gain due to emission. Before we derive the [RTE](#), we first define some terms and physical quantities.

The first term is spectral irradiance, L_ν . Spectral irradiance is defined as the energy flow in a direction \mathbf{n} , for a solid angle $d\Omega$, per unit time per unit temporal frequency bandwidth. Irradiance is defined as the spectral irradiance over a small frequency range $[\nu, \nu + \Delta\nu]$:

$$L(\vec{r}, \hat{s}, t) = L_\nu(\vec{r}, \hat{s}, t)\Delta\nu \quad (1.2)$$

Where:

\vec{r} is the position;

\hat{s} is the unit normal vector;

t is the time;
and $L(\vec{r}, \hat{s}, t)$ is the irradiance [$W \cdot m^{-2} \cdot sr^{-1}$].

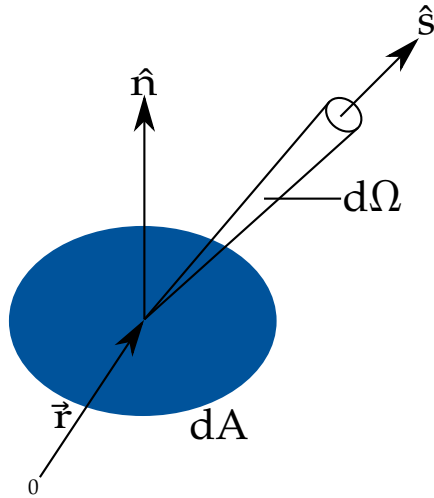


Figure 1.3: Energy flow through area dA within solid angle $d\Omega$ in a direction \hat{s} . Adapted from [16, 17]

The irradiance can be used to determine the energy, dE , transported across an area dA , in a solid angle $d\Omega$ in a time dt (see Fig. 1.3) is:

$$dE = L(\vec{r}, \hat{s}, t) \cdot (\hat{s} \cdot \hat{n}) dAd\Omega dt \quad (1.3)$$

Where:

\hat{n} is the unit normal to dA ;
and $\hat{s} \cdot \hat{n}$ is the angle of the solid angle.

Irradiance can also be used to determine the fluence rate, ϕ , which is defined as the energy flow per unit time, independent of the flow direction.

$$\phi(\vec{r}, t) = \int_{4\pi} L(\vec{r}, \hat{s}, t) d\Omega \quad (1.4)$$

Where:

ϕ is the fluence rate [$W \cdot m^{-2}$].

Irradiance is also the main variable in the RTE, as it describes the light distribution throughout the medium, and by solving the RTE yields the irradiance, which in turn gives information on the state of the system and all the physical properties of it.

With the irradiance defined, as well as the other quantities that follow, we can now derive the RTE [16, 17]. We first consider conservation of energy, as shown in Eq. (1.5).

$$dP = -dp_{div} - dp_{ext} + dP_{scatt} + dP_{src} \quad (1.5)$$

Where:

dP is the total change in energy in the volume $dAds$ within the solid angle, $d\Omega$, per unit time (see Fig. 1.4);

dp_{div} is the energy loss due to the divergence of the radiation beam per unit time;

dP_{ext} is the energy loss due to absorption and scattering within $dAdsd\Omega$;
 dP_{scatt} is the energy gain due to scattering from \hat{s}' into $d\Omega$ per unit time;
and dP_{src} is the energy gain due to emission within the medium, per unit time.

The total change in energy in the volume element within the solid angle $d\Omega$, dP , is equal to:

$$dP = \frac{1}{c} \frac{\partial L(\vec{r}, \hat{s}, t)}{\partial t} dAdsd\Omega \quad (1.6)$$

Where c is the speed of light.

The first loss term, dP_{div} , is the energy loss due to divergence of the radiation beam. This is modelled as:

$$dP_{div} = \frac{\partial L}{\partial s} d\Omega dV \quad (1.7)$$

$$= \hat{s} \cdot \nabla L(\vec{r}, \hat{s}, t) d\Omega dV \quad (1.8)$$

dP_{ext} is the second loss term, and accounts for energy loss due to scattering and absorption in the volume element within the solid angle $d\Omega$. This is modelled as:

$$dP_{ext} = \mu_t ds L(\vec{r}, \hat{s}, t) dAd\Omega \quad (1.9)$$

The first energy gain term, dP_{src} , is due to emission in the volume element within the solid angle $d\Omega$.

$$dP_{src} = S(\vec{r}, \hat{s}, t) dV d\Omega \quad (1.10)$$

The second energy gain term, and final term, is due to the incident energy on the volume element within the solid angle $d\Omega$ in direction \hat{s} due to scattering from any direction \hat{s}' .

$$dP_{scatt} = N_s dV \left(\int_{4\pi} L(\vec{r}, \hat{s}', t) P(\hat{s}', \hat{s}) \sigma_s d\Omega' \right) d\Omega \quad (1.11)$$

$$= \mu_s dV \left(\int_{4\pi} L(\vec{r}, \hat{s}', t) P(\hat{s}', \hat{s}) d\Omega' \right) d\Omega \quad (1.12)$$

Where:

N_s is the number density of scatters;

$P(\hat{s}', \hat{s})$ is the scattering phase function (see Section 1.4 for further discussion);

and σ_s is the cross section of the scatters, thus $\mu_s = N_s \sigma_s$ (again see Section 1.4 for further discussion).

Finally substituting Eqs. (1.6), (1.8) to (1.10) and (1.12) into Eq. (1.5) yields the RTE:

$$\frac{1}{c} \frac{\partial L(\vec{r}, \hat{s}, t)}{\partial t} + \hat{s} \cdot \nabla L(\vec{r}, \hat{s}, t) = -\mu_t L(\vec{r}, \hat{s}, t) + \mu_s \int_{4\pi} p(\hat{s}, \hat{s}') L(\vec{r}, \hat{s}', t) d\Omega' + S(\vec{r}, \hat{s}, t) \quad (1.13)$$

In general, the RTE is hard to solve in arbitrary 3D geometries, however there are a number of approximations, and numerical methods available. Diffusion approximation, Kubelka-Munk Theory (K-M theory), and MCRT are the common methods used to approximate the RTE.

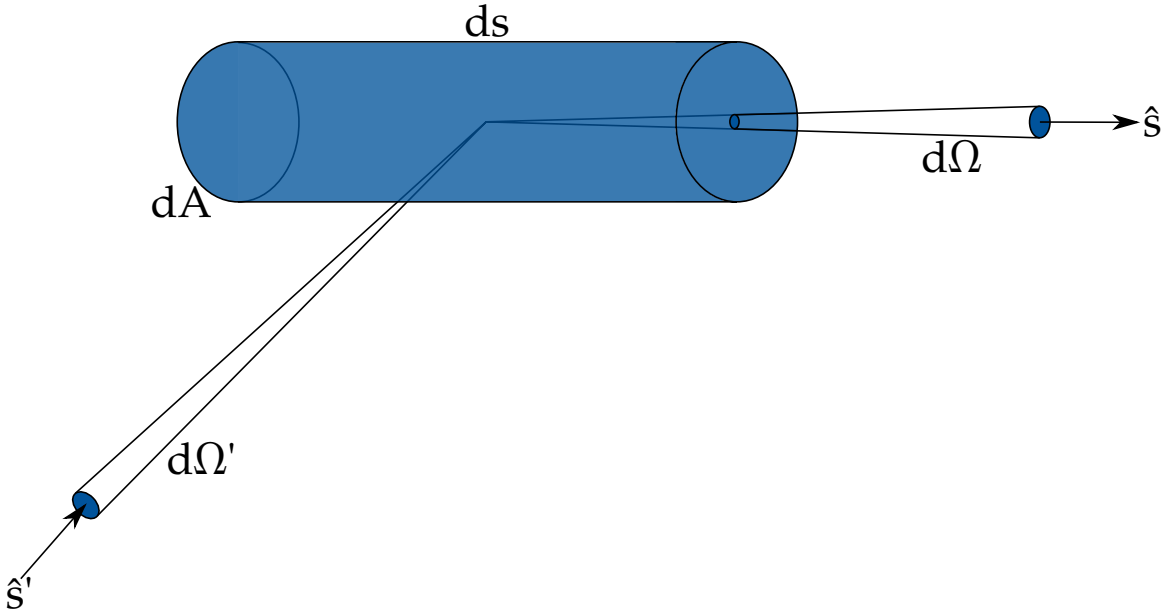


Figure 1.4: Cylindrical volume element, $ds \cdot dA$, with solid angle $d\Omega$ in direction \hat{s} and solid angle $d\Omega'$ in direction \hat{s}' . Energy flowing through this element is used to derive the RTE. Adapted from [16, 17].

Kubelka-Munk theory K-M theory was originally developed in order to calculate the light distribution in thin layered materials, such as paint or paper [18]. The theory is rather simple and makes many assumptions about the medium and the incident light. The main assumptions of K-M theory are: only scattering and absorption take place in the medium, the incident light is already diffuse, the medium is uniform, only isotropic scattering, no external or internal reflections, and the medium is planar and infinitely wide [19–21].

These assumptions make K-M theory, very poor for modelling light-tissue interactions. This is as in tissue, scattering is not isotropic, but rather forward biased (see Section 1.4). Tissue is rarely, if ever, planar and infinitely wide. Tissue also has some reflections at its external and internal boundaries, due to change in refractive indices. Many medical and biophotonic treatments/methods use laser light which is not diffuse. Finally tissue can also exhibit fluorescence, which K-M theory is not able to model, along with polarization. K-M theory does have some positive aspects. It is good at calculating the diffuse reflectance of simple mediums, and can be used to roughly estimate calculations. Though it is not well suited for modelling light-tissue applications.***refs for these claims***

Diffusion approximation The diffusion approximation for the RTE, is where the irradiance is separated into two components:

$$L(\vec{r}, \hat{s}) = L_c(\vec{r}, \hat{s}) + l_d(\vec{r}, \hat{s}) \quad (1.14)$$

Where L_c is the unscattered contribution, which satisfies Beer's law*, and L_d is the diffuse contribution. The L_d component is expanded using Legendre polynomials and truncated. The

*Beer's law (or Beer-Lambert law) states that the transmission, T , is equal to $e^{-\mu L}$, where L is the distance and μ is the attenuation coefficient.

diffusion approximation also has a number of assumptions and restrictions. The main assumption is that scattering dominates over absorption, and that the scattering is nearly isotropic. This restricts the types of scattering the Diffusion approximation can model, though using similarity relations can partially model scattering in tissue [22, 23].

Diffusion theory is computationally fast, and simple. However it is poor at modelling light-tissue interactions due to its assumptions and restrictions, mainly the inaccurate modelling near the boundaries of the medium and its lack of modelling fluorescence and other microphysics. However it can be used to speed up MCRT in optically thick regions [24, 25].

The final method, MCRT, is a method that is numerically equivalent to the RTE [16]. MCRT is a very flexible method, it can model arbitrary 3D geometries, various microphysics: fluorescence, and polarisation. It can also model various different light sources, from collimated laser beams, to diffuse light sources. The only downside that is noted in the literature is that the MCRT can be very expensive computationally. However with computational power growing faster with each year, this is less and less of a problem going forward. The next several sections give an in depth description of the MCRT method and its flexibility, along with a description of the code used in this thesis to solve various medical and biophotonic problems.

1.2.2 MCRT algorithm

The MCRT algorithm can be as simple as a ~ 20 line program to as complex as needed for the problem at hand. This section will provide a detailed description a simple MCRT algorithm for a 3D voxel based grid.

1.2.2.1 Grid set-up

The first step of the MCRT algorithm is to set-up the grid which acts as the simulated medium. This grid consists of $n \times n \times n$ voxels[†] of which each voxel has its own optical properties (see Section 1.4 for discussion). This allows the medium of interest to be discretised onto a grid, which gives a good approximation of the real-life medium (see Section 1.5 for discussion on this), along with setting up the medium, arrays which store the locations of the voxel walls in each cardinal direction are created for reference in later parts of the code. Once the medium has been set-up photon packets are launched and propagated through the voxel structure.

1.2.2.2 Photon launch

The initial step (besides medium set-up and other book keeping) of any MCRT algorithm is to launch a photon packet. Depending on the source of photon packets for a given simulation, this step varies from simulation to simulation. The general idea of launching a photon packet is that the packet is given an initial direction vector and position (which consists of a physical position and a voxel position)[‡]:

$$direction = \begin{bmatrix} n_{xp} \\ n_{yp} \\ n_{zp} \end{bmatrix} \quad (1.15)$$

$$position = [x_p, y_p, z_p] \quad (1.16)$$

$$voxel = [x_{cell}, y_{cell}, z_{cell}] \quad (1.17)$$

[†]A voxel is a 3D pixel

[‡]all variables given in this section are the same as they are in the code.

In order to set the direction vectors, the components of the direction vectors must be first set. The packets position is tracked using a Cartesian coordinate system, however for ease of computation for calculating scattering angles (see Section 1.2.2.4), the direction vectors are computed in a spherical system thus the direction vectors are:

$$n_{xp} = \sin(\theta) \cdot \cos(\phi) \quad (1.18)$$

$$n_{yp} = \sin(\theta) \cdot \sin(\phi) \quad (1.19)$$

$$n_{zp} = \cos(\theta) \quad (1.20)$$

θ and ϕ are generated dependant on the photon source used. The individual sine and cosine terms are saved for use in the scattering routines, see Section 1.2.2.4.

1.2.2.3 Photon move

The next step in the algorithm is moving a packet to the next interaction point. The probability a packet will interact over a distance dL is $\mu_t dL$, where μ_t is the interaction probability (see Section 1.4). Thus the probability of travelling dL without any interaction is $1 - \mu_t dL$. Therefore over a distance L , with N segments of length L/N the probability of travelling L before any interaction:

$$P(L) = (1 - \mu_t \frac{L}{N}) \cdot (1 - \mu_t \frac{L}{N}) \dots (1 - \mu_t \frac{L}{N}) = (1 - \mu_t \frac{L}{N})^N \quad (1.21)$$

$$P(L) = \lim_{N \rightarrow \infty} (1 - \mu_t \frac{L}{N})^N = e^{-\mu_t L} = e^{-\tau} \quad (1.22)$$

Where τ is the number of mean free paths over a distance L . We now have a PDF, Eq. (1.22), for the distance a packet will travel before an interaction occurs. For this to be of use we need to be able to sample from this PDF in order to get a random optical depth. Using the Monte Carlo method described in Section 1.1.1, with ξ as our random variable, we get:

$$\xi = \int_0^\tau e^{-\tau'} = 1 - e^{-\tau} \rightarrow \tau = -\log(1 - \xi) \quad (1.23)$$

As ξ is symmetric about 0.5 we can substitute $1 - \xi$ for ξ yielding:

$$\tau = -\log(\xi) \quad (1.24)$$

We now have an optical distance, however we need to convert this into a physical distance so that we can move our photon packet. From our definition of τ we know that $\tau = \int_0^L \mu_t dS$, and if we have a smooth, homogeneous medium (i.e not a gridded medium) thus

$$L = \frac{\tau}{\mu_t} \quad (1.25)$$

Therefore in order to update the packets position is simply:

$$x_p = x_p + L \cdot n_{xp} \quad (1.26)$$

$$y_p = y_p + L \cdot n_{yp} \quad (1.27)$$

$$z_p = z_p + L \cdot n_{zp} \quad (1.28)$$

However as the code in this thesis is a 3D gridded Cartesian code, we have to slightly adjust how we move and update the packets position. As stated in Section 1.2.2.1, the medium has been discretised onto a grid, so that each voxel can have a different μ_t , thus Eq. (1.25) becomes:

$$L = \frac{\tau}{\mu_{t,\zeta}} \quad \zeta = (x, y, z) \quad (1.29)$$

with $\mu_{t,\zeta}$ the μ_t for the ζ^{th} voxel. The position is then updated as before using Eqs. (1.26) to (1.28). The next step in the algorithm is the interaction event, which can consist of either: scattering, absorbing or fluorescing.

1.2.2.4 Photon scatter and absorbing

The first part of this section of the algorithm is to decide what kind of interaction the packet has with the medium. This section will focus on scattering and absorbing with other interaction events left for the chapters that detail these behaviours.

To decide whether a packet scatters or absorbs involves ‘throwing’ a random number and comparing it against the albedo. As detailed in Section 1.4 the albedo is the scattering probability $a = \frac{\mu_a}{\mu_a + \mu_s}$. The random number is compared to the albedo, and if the random number is less than the albedo then the packet scatters, otherwise the packet is absorbed.

Packet absorption

If the interaction event is a photon packet absorption, then the algorithm terminates the photon packets and starts the next photon packet, Section 1.2.2.5.

Packet scattering

If the interaction event is a packet scattering, then the packet is scattered into a new direction and the above process are carried out until a termination clause is met, see Section 1.2.2.5.

Depending of the medium being simulated, it can either be isotropically scattering or preferentially scattering in a direction. In the case of simulating photon propagation in tissue, tissue is highly forward scattering.

Anisotropy is the degree of deviation in the photon packets path at each interaction event. The measure of anisotropy is the g value, g . With g taking any value from -1 to 1 , -1 is highly backward scattering, 0 is isotropic scattering and 1 is highly forward scattering.

1.2.2.5 Termination

1.2.3 Code details

This section details the the actual implementation of the MCRT algorithm detailed in the previous section, along with any computational necessities and speed ups on the original algorithm.

1.3 Validation of MCRT code

1.4 Optical properties

Optical properties of a medium are the properties that determine how light is transported though that medium. Usually the optical properties of a medium are defined by four main parameters:

the scattering and absorption coefficients (μ_s and μ_a), the anisotropy coefficient (g), and the refractive index (n). There are several other optical properties the medium can be defined with, however these in general are only used for specific applications, such as Raman cross-sections.

1.4.1 Scattering

The scattering coefficient, along with the anisotropy value (see Section 1.4.2), define how light is transported through a medium. Scattering in skin is due to a number of different scatterers, and inhomogeneities within the skin. The main scatterers are filamentous proteins such as collagen, and elastin which are generally found within the dermis, and epidermis and both are composed of long filament like bundles ***ref 7***. In the upper layers of the skin the main scatterers are keratins and various chromophores such as melanin. These scatterers and their size determine how light is scattered, and in which direction into.

The scattering of light within tissue is usually defined as μ_s or μ'_s : the scattering coefficient and the reduced scattering coefficient, where $\mu'_s = \mu_s(1-g)$. The scattering coefficient is defined such that the probability of transmission without scattering in a path length L is:

$$T = e^{-\mu_s L} \quad (1.30)$$

This gives units of inverse length for the scattering coefficient (usually measured in cm^{-1}). The reduced scattering coefficient is quite often given in place of the scattering coefficient, as the reduced coefficient is more easily measured than the ‘normal’ coefficient [26].

1.4.2 Anisotropy

Anisotropy describes the degree of deviation in the photon path at each scattering event. The anisotropy value is taken from the phase function for the medium. The phase function, $\Phi(\theta, \phi)$, is usually normalised over all angles:

$$\int_{\Omega} \Phi(\theta, \phi) d\Omega = 1 \quad (1.31)$$

Where θ , and ϕ are the usual spherical angles. Thus Rayleigh and isotropic scattering’s phase functions are:

$$\Phi_{isotropic}(\theta, \phi) = \frac{1}{4\pi} \quad (1.32)$$

$$\Phi_{Rayleigh}(\theta, \phi) = \frac{3}{8\pi}(1 + \cos^2(\theta)) \quad (1.33)$$

Phase functions are hard to experimentally determine for biological tissues ***ref***, therefore the phase function is usually cast as the anisotropy value g , which is defined as the average angle of deflection:

$$g = \langle \cos(\theta) \rangle = \int_{\Omega} \cos(\theta) \Phi(\theta, \phi) d\Omega \quad (1.34)$$

The anisotropy factor, g , can take on any value from -1 to 1 . Where a value of -1 is highly backward scattering, 0 is isotropic scattering and 1 is highly forward scattering.

There are various phase functions that can be used to model the anisotropy factor in medium, but the standard phase function for scattering in a biological tissue is the Henyey-Greenstein phase function. The Henyey-Greenstein phase function is shown in Eq. (1.35):

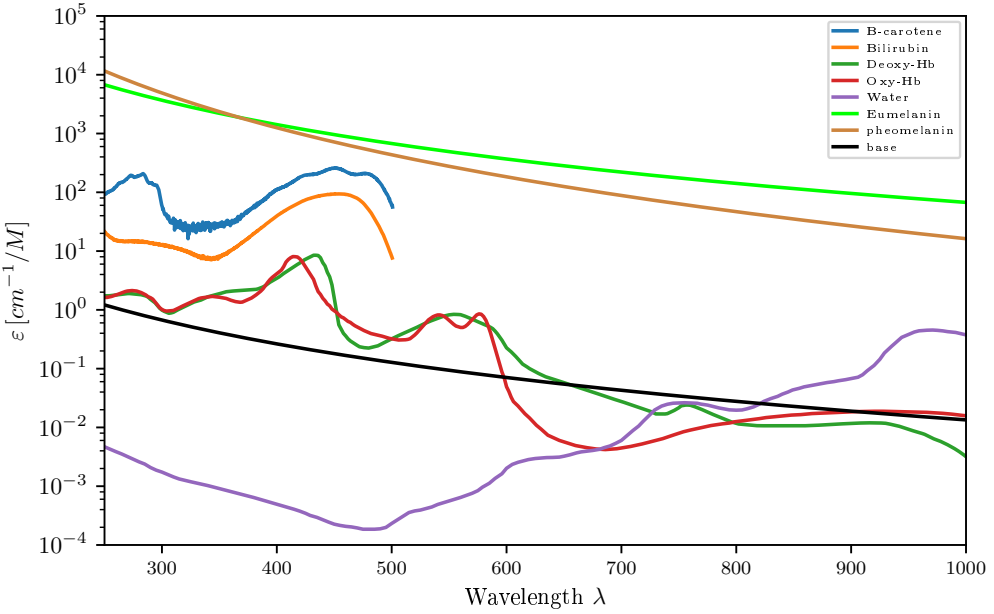


Figure 1.5: Spectra of some of the more common absorbers found in the skin.

$$\Phi_{H.G}(\theta, \phi) = \frac{1}{4\pi} \frac{1 - g^2}{(1 + g^2 - 2g \cos(\theta))^{\frac{3}{2}}} \quad (1.35)$$

The Henyey-Greenstein phase function was originally used as the phase function for scattering in dusty galactic clouds, but has since become the *de-facto* phase function for scattering in biological tissue***ref***. The Henyey-Greenstein phase function is regarded as a ‘good’ phase function for biological tissues as it can model forward scattering, which tissue exhibits, and it is relatively simple to implement [27].

1.4.3 Absorption

The absorption within biological tissues is defined by the absorption coefficient μ_a . The absorption coefficient is defined, like the scattering coefficient, by considering the probability of transmission without absorbing in a path length L:

$$T = e^{-\mu_a L} \quad (1.36)$$

This, again like the scattering coefficient, gives inverse distance for the unit of the absorption coefficient (and its is also usually measured in units of cm^{-1}).

There are various sources of absorbers in tissue: blood, water, fat, melanin, β -carotene, bilirubin are among the more absorbing chromophores. These chromophores can all contribute, depending on the probing wavelength, with some more absorbing than others, see Fig. 1.5.

1.4.4 Refractive index

1.4.5 Other parameters

There are various other optical parameters that can define a medium, including: Raman cross sections, fluorescence quantum yields, polarization cross sections.

1.5 Further extensions to the code

This section details the miscellaneous additions to the MCRT algorithm that the various chapters in this thesis may or may not use.

1.5.1 Fresnel reflections & refractions

this section in madrid work?

$$R_s = \left| \frac{n_1 \cos\theta_i - n_2 \cos\theta_t}{n_1 \cos\theta_i + n_2 \cos\theta_t} \right|^2 \quad (1.37)$$

$$R_p = \left| \frac{n_1 \cos\theta_t - n_2 \cos\theta_i}{n_1 \cos\theta_t + n_2 \cos\theta_i} \right|^2 \quad (1.38)$$

1.5.2 Parallelisation of the MCRT algorithm

As mentioned in the previous sections, MCRT can be computationally intensive, especially when dealing with highly scattering mediums. Fluorescence can also cause simulations times to drastically increase as photons are no longer ‘killed’ off, but rather re-emitted at a new wavelength. Other optical processes such as Raman scattering are highly unlikely events, which again can lead to a dramatic increase in simulation times, as many photons are required to be simulate in order to get ‘good’ statistics.

Fortunately MCRT is classed as an ‘embarrassingly parallel’ problem[§]. This means that it is trivial to parallelise in comparison to other algorithms. The reason that MCRT is classed as ‘embarrassingly parallel’, is that the algorithm can be split up onto separate processes, with no little need for communication between them. In reality this means that n copies of the algorithm can run on n cores in a processor, with communication taking place at the start and end of each simulation run.

All the code in this thesis is parallelised using Message-passing interface (MPI), with the only communication taking place at the end, where the path length estimators are collated on to all process.

ToDo do parallel tests finish writing this subsection ***ToDo***

1.6 Improving the voxel tissue model

Needed?

As voxels are cuboid in shape, in order for them to accurately model biological tissue, which is decidedly not smooth, new methods or approximations were attempted to improve the modelling

[§]However this is not true for all MCRT applications. For example using the Bjorkman & Wood [28] immediate temperature corrections method, turns MCRT into a different class of parallel problem [29].

of biological tissue. The first is bump-mapping, a technique borrowed from computer graphics. The second is to dispense with the voxel model and use a triangular based mesh. Both these methods were tried during the course of this thesis, but were abandoned due to time constraints. This section gives a brief overview of these techniques and why they were not ultimately used in this thesis.

Chapter 2

Computational modelling of tissue ablation

2.1 Introduction and background

Lasers are used in wide variety of medical procedures not limited to: coagulating scalpels, port wine stain removal, tattoo removal, hair removal, and skin rejuvenation [30–34]. One class of laser used in these procedures are ablative lasers. Ablative lasers are usually high powered lasers targeted at a specific chromophore in the skin, to partially or fully remove layers of skin. These types of lasers are commonly used for aesthetic procedures such as: skin rejuvenation [34], and removal of various diseases such as Rhinophyma [35] or lesions/nodules [36]. Ablative lasers have also been recently investigated as a means of better drug penetration into the skin for various therapies such as [photo-dynamic therapy \(PDT\)](#). The ablative laser ‘drill’ holes in the skin, which allows topical treatments to better diffuse into the skin [37].

One downside to using lasers to remove tissue, is that unlike a scalpel, where the surgeon has full control of the depth of the incision, ablative lasers are not as predictable. Lasers can also cause thermal damage to the surrounding areas, leading to potentially unwanted effects, though some applications of ablative lasers utilise the thermal damage, particularly aesthetic procedures [38].

Currently the only reliable method to measure the depth of the ablative holes, is via a biopsy, which is an invasive procedure. We propose to use [optical coherence tomography \(OCT\)](#) to measure the ablative crater non-invasively *in-vivo*. The [OCT](#) measurements are then compared to by a computational model. This computational model could be used to predict the depth of the ablative crater when using a certain laser power for various different applications such as: laser assisted drug delivery, and various cosmetic applications.

This chapter examines using [MCRT](#) techniques coupled to a heat transfer simulation, in order to study the thermal damage to tissue due to fractional lasers. Fractionated ablative lasers are ablative lasers where the power is spread over several beams, such as to leave viable tissue around zones of damaged/necrotic tissue [39]. We present experimental work carried out on porcine tissue by our collaborators at the University of Dundee and the photobiology department at Ninewells hospital, along side our computational model of tissue ablation.

2.2 Methods

In order to replicate the experimental work *in silico*, our numerical model has three main portions. The first is the **MCRT** that models light transport through tissue so that we can calculate the laser energy deposited as a function of time and space. The second, a **finite difference method (FDM)** which is used to calculate the heat diffusion within the tissue due to the absorbed laser energy. Finally, a tissue damage model to track the tissue damage caused by the laser. All these individual portions are connected together to create our numerical model. This chapter explains in detail each portion of the numerical model used to simulate tissue ablation via a laser.

2.2.1 Monte Carlo radiation transport (MCRT)

This part is here as it will be needed for paper. probably not needed in chapter though... **MCRT** is the ‘gold standard’ for simulating the transport of light through biological tissue [40, 41]. This is due to its flexibility in modelling 3D geometries, various light sources, and micro-physics, such as fluorescence. It uses interaction probabilities and random numbers in order to model the ‘random walk’ that photons undergo in a turbid medium. We simulate the propagation of photon packets, which represent photons with a given power, derived from the incident radiant source. These ‘packets’ can undergo scattering, absorption and fluorescence, and polarisation [13, 42, 43]. **MCRT** has been used to model light-tissue interactions in many different medical and biophotonic applications [44–46]. **MCRT** is used here to calculate the energy deposited by the laser, which is then passed to the heat transport simulation.

The original **MCRT** code was developed for astronomy applications [13, 47], and has since been adapted for use in the medical field [44, 48].

The tissue medium for the **MCRT** and heat transport simulations is a 3D voxel model (Fig. 2.1). This allows the variation of optical and thermal properties from voxel to voxel, making it the ideal type of grid for modelling tissue ablation. We use $160 \times 160 \times 160$ voxels, representing a tissue sample size of $0.06 \times 0.06 \times 0.18\text{ cm}$. We assume the porcine skin is uniform, so initially our voxel model is uniform, and the optical properties of porcine skin at the wavelength of interest is mainly that of water mixed with protein [49], see Fig. 2.10.

Figure 2.2. shows the overall algorithm for the simulation, including the **MCRT** portion. The **MCRT** portion of the algorithm begins with determining where the photon enters the medium. This is calculated by randomly selecting one of the pixel beams, from the 9×9 array of pixel beams. Next the position on the surface of the medium is calculated. As the exact profile of the pixel beams are unknown, we assume them to be uniformly circular. Thus, the packets position is uniformly sampled on a circle the width of the pixel beam.

Once the packet enters the simulation, a propagation distance for the packet is calculated using Eq. (2.1). The packet then moves this distance before undergoing an interaction event. This can be either scattering or absorption, however in this simulation absorption dominates, and thus we assume no scattering takes place. This process is repeated until the photon has either been absorbed or exits the medium.

$$L = -\frac{\ln(\xi)}{\mu_a} \quad (2.1)$$

Where:

ξ a random number ($\tau = -\ln(\xi)$, τ is the optical depth);

μ_a is the absorption coefficient;

L is the physical distance.

Equation (2.1) is the equation for a uniform medium. As the medium we are simulating changes over time due to thermal damage this equation has to be adapted for a 3D Cartesian

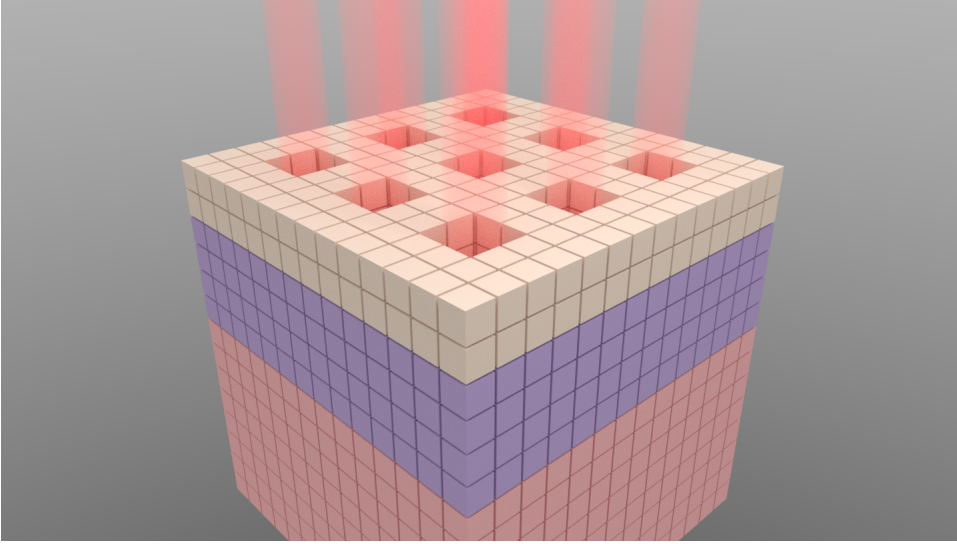


Figure 2.1: Example of a possible voxel model, with three different layers, various holes due to ablative pixel beam lasers. Each voxel can represent a different optical/thermal property of the tissue medium.

grid. Each voxel can have different optical properties, thus the photon packet is moved on a voxel by voxel basis. To start the movement process, a random number is generated, which is used to sample an optical depth the photon packet will travel. Next the photon enters the voxel and the maximum distance the photon can travel in the new voxel is calculated along the photon's trajectory. If this optical distance is less than the optical depth sampled, then the photon enters the next voxel. If the distance is larger than the sampled optical distance then the photon has an interaction event in that voxel. The photon packet moves to the interaction event in the voxel and then undergoes scattering or absorption. The whole process is repeated until the photon 'dies' via absorption or leaving the medium. This in turn is again repeated for all the photons, until all the photons have been absorbed or have escaped the tissue medium. We use 1 million photon packets per MCRT simulation run.

To calculate the energy absorbed in the porcine tissue via the laser we use the path length counter method devised by Lucy [50] (see Fig. 2.3). The energy absorbed per voxel is therefore calculated as:

$$E_i^{abs} = \frac{P}{NV_i} \sum \mu_{a,i} s \quad (2.2)$$

Where:

P is power [W];

N is the number of photons;

V_i is the volume of the i^{th} voxel [m^{-3}];

$\mu_{a,i}$ is the absorption coefficient of the i^{th} voxel [cm^{-1}];

and s is the pathlength of a photon packet through the i^{th} voxel [cm].

This grid of absorbed energy is then passed to the heat transport portion of the simulation, so that the heat diffusion in the porcine tissue can be calculated.

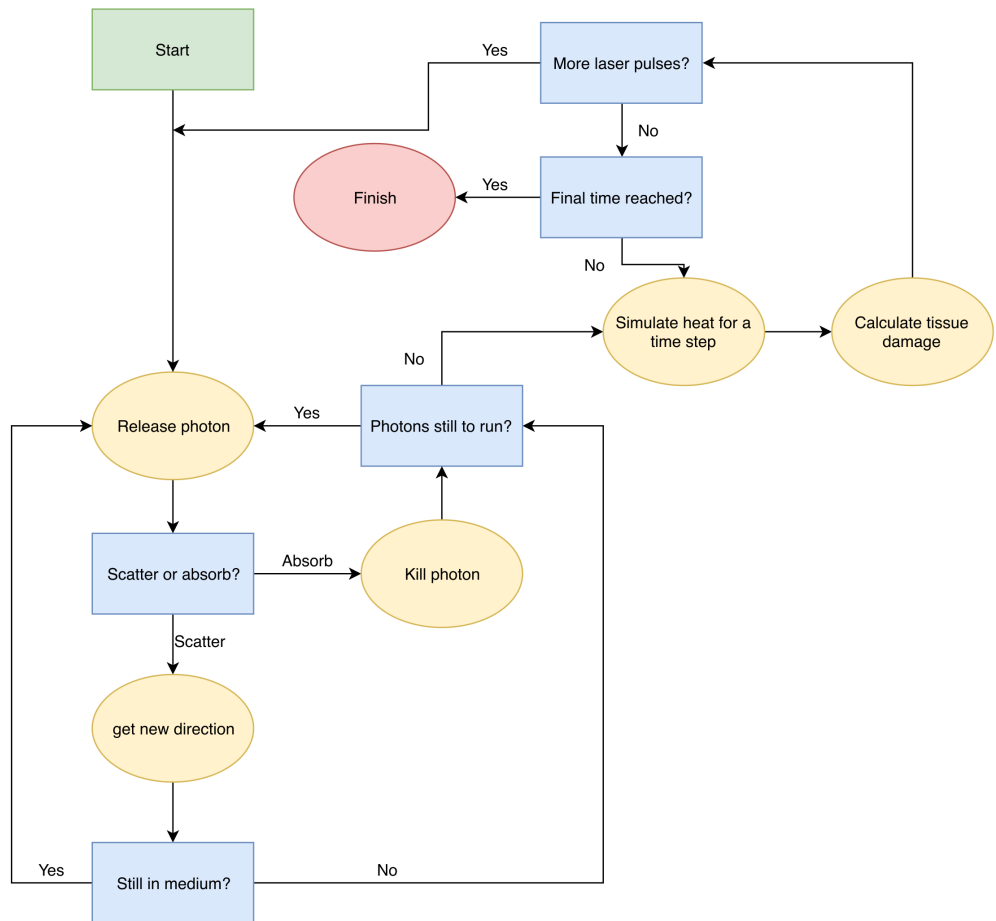


Figure 2.2: Flowchart of the tissue ablation algorithm.

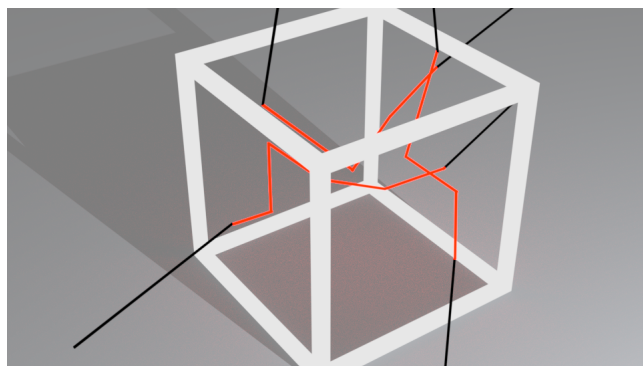


Figure 2.3: Red lines are photon paths within a voxel. Black lines photon paths out with the voxel. Red photon paths, weighted by μ_a , are summed up in order to calculate the absorbed energy within each voxel.

2.2.2 Heat transport

The diffusion of heat can be modelled using the heat equation (Eq. (2.3)), which is derived from Fourier's law and the principle of conservation of energy [51] (see Appendix A). The standard heat equation is a partial differential equation of the parabolic form. Solutions and analytical methods are readily available for lower dimensions (i.e. 1D heat diffusion), but for higher dimensions such as three dimensions, numerical models must be used for all bar the simplest problems. The simplest form of the heat equation is shown below:

$$\rho c_p \frac{\partial T}{\partial t} = \nabla \cdot (\kappa \nabla T) + \dot{q} \quad (2.3)$$

Where:

- $T(x, y, z, t)$ is the temperature as a function of time and space [K];
- κ is the thermal conductivity [$W \cdot m^{-1} \cdot K^{-1}$];
- ρ is the density [$Kg \cdot m^{-3}$];
- c_p the specific heat capacity [$J \cdot K^{-1}$];
- $\dot{q}(x, y, z, t)$ is the source/sink term as a function of time and space [$W \cdot m^{-3}$].

Equation (2.3) is for a homogeneous system where the thermal properties do not change as function of time, space and/or temperature. However in order to model a moving ablation front we must therefore use the non-linear heat equation where the thermal properties can be a function of time, space and/or temperature (Eq. (2.4)).

$$\frac{\partial T}{\partial t} = \frac{1}{(\rho c_p)_\xi} (\nabla k_\xi T + k_\xi \nabla^2 T) + \dot{q} \quad \xi = (i, j, k) \quad (2.4)$$

We have also included in the Eq. (2.4) a source and sink term to allow the modelling of heat loss/gain from external sources/sinks. The \dot{q} term is a heat source/sink term. The heat source in this simulation is due to the laser, and we assume the only loss of heat to the surrounding medium is via convection and conduction.

These boundary conditions must be considered. All faces of the cube, bar the laser facing face, are considered to be pinned at $5^\circ C$, as the porcine skin was kept cooled prior to experimental work and the simulation volume is smaller than the porcine tissue samples. The laser facing face has a simple convective BC (based upon Newtons law of cooling):

$$\dot{q}_c = -hA(T - T_\infty) \quad (2.5)$$

Where:

- h is the heat transfer coefficient [$W \cdot m^{-2} \cdot K$];
- A is the area of the grid element, that is radiating/convicting heat away [m^{-2}];
- and T , and T_∞ are the temperature in a voxel and the surrounding medium temperature respectively [K].

As Eq. (2.4) is generally hard to solve in arbitrary geometries with complex boundary conditions we employ a numerical method to solve Eq. (2.4). The numerical method we employ is a **FDM**. The FDM is derived from the Taylor series approximation for derivatives, see Eq. (2.6).

A function $f(x)$ is discretised onto a grid with N nodes a distance Δx apart (see Fig. 2.4). We can then truncate and rearrange Eq. (2.6) and assume that the remainder term R_1 is sufficiently small enough, to yield an approximation for the first derivative of a function $f(x)$ at a point $x_0 + \Delta x$, see Eq. (2.7). Crefeqn:fdfirst is the so called forward difference, due to it using a point in the 'forward' direction. We can also calculate the 'backward' and central difference terms by using a node at $x_0 - \Delta x$ for the backward difference Eq. (2.8b). The central difference (Eq. (2.8c))

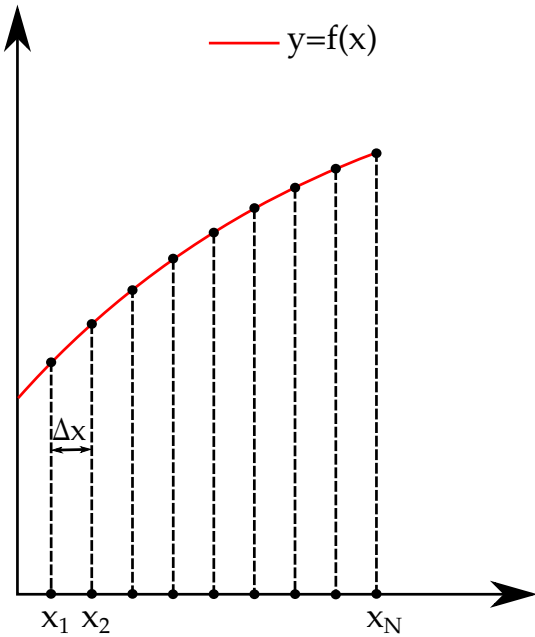


Figure 2.4: Discretisation of $f(x)$.

is an average of the forward and backwards differences. We can also give expressions for the 2^{nd} derivatives for backward, forward and central (forward and backward 2^{nd} order equations omitted for brevity) Eq. (2.8d).

$$f(x_0 + \Delta x) = f(x_0) + \frac{f'(x_0)}{1!} \Delta x + \frac{f''(x_0)}{2!} \Delta x^2 + \dots + \frac{f^{(n)}(x_0)}{n!} \Delta x^n + R_n(x) \quad (2.6)$$

$$f'(x_0) \approx \frac{f(x_0 + \Delta x) - f(x_0)}{\Delta x} \quad (2.7)$$

$$\frac{df}{dx} = \frac{f_{i+1} - f_i}{\Delta x} * \quad (forward) \quad (2.8a)$$

$$\frac{df}{dx} = \frac{f_i - f_{i-1}}{\Delta x} \quad (backward) \quad (2.8b)$$

$$\frac{df}{dx} = \frac{f_{i+1} - f_{i-1}}{2\Delta x} \quad (central) \quad (2.8c)$$

$$\frac{d^2 f}{dx^2} = \frac{f_{i-1} - 2f_i + f_{i+1}}{\Delta x^2} \quad (central) \quad (2.8d)$$

Thus the linear heat equation Eq. (2.3), in 1D, taking a 1^{st} order forward time derivative,

*For brevity we define $f(x_0 + \Delta x)$ as f_{i+1} , $f(x_0 - \Delta x)$ as f_{i-1} , etc.

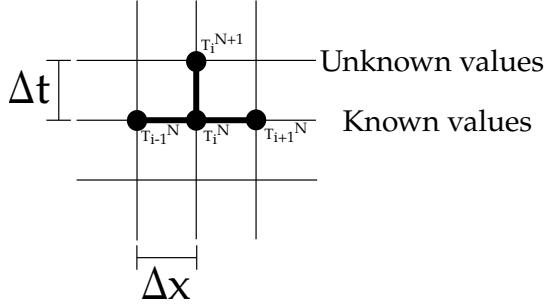


Figure 2.5: Finite difference method stencil for simple explicit scheme

and a 2nd order central spatial derivative gives:

$$\frac{T_i^{n+1} - T_i^n}{\Delta t} = \alpha \frac{T_{i-1}^n - T_i^n + T_{i+1}^n}{\Delta x^2} + \frac{\dot{q}}{\rho c_p} \quad (2.9a)$$

$$T_i^{n+1} = \alpha \Delta t \frac{T_{i-1}^n - 2T_i^n + T_{i+1}^n}{\Delta x^2} + \frac{\Delta t \dot{q}}{\rho c_p} \quad (2.9b)$$

Where $\alpha = \frac{\kappa}{\rho c}$.

Equation (2.9b) is called the ‘simple explicit form of finite-difference approximation’ [52]. Figure 2.5 shows the ‘stencil’ of this scheme, where there are three known points at time N , and just one unknown at time $N+1$. There are various other scheme that can be used to calculate the temperature at the the next time step. However we use a simple explicit scheme here, due to its ease of implementation despite there being a constraint on the stability in comparison to an implicit method. This method is also easily scaled up to 3D with little difficulty.

For the more complicated non-linear heat equation we have to account for the possibility that the medium is not continuously smooth between nodes, in terms of optical and thermal properties. The two easiest methods [52] of achieving this are: One, lag the value behind by one step, i.e $c_p^{n+1} = c_p^n$. Two, average κ , ρ , and c_p using a half difference scheme where the thermal property used in the calculation is the thermal property half way between two nodes, i.e the average of the two nodes:

$$\kappa^\pm = \frac{\kappa_i + \kappa_{i\pm 1}}{2} \quad (2.10)$$

$$\rho^\pm = \frac{\rho_i + \rho_{i\pm 1}}{2} \quad (2.11)$$

$$c_p^\pm = \frac{c_{p,i} + c_{p,i\pm 1}}{2} \quad (2.12)$$

Thus for the simple 1D case as in Eq. (2.9b), we average the thermal properties when computing the coefficients of the temperature nodes, and lag the thermal properties when adding the heat from the laser:

$$T^{N+1} = \Delta t (A T_{i-1}^N - 2B T_i^N + D T_{i+1}^N) + T_i^N + \frac{\Delta t q_L}{\rho c_p} \quad (2.13)$$

Where (in the x direction):

$$\begin{aligned} A &= \frac{\kappa^-}{\rho^- c_p^- 2\Delta x^2} \\ B &= \frac{\kappa^+}{\rho^+ c_p^+ 2\Delta x^2} \\ D &= \frac{(A + B)}{2} \end{aligned} \quad (2.14)$$

Equation (2.13) can be generalised to higher dimensions easily. The 3D case gives:

$$U_{xx} = (AT_{i-1,j,k}^N - 2BT_{i,j,k}^N + DT_{i+1,j,k}^N) \quad (2.15)$$

$$U_{yy} = (AT_{i,j-1,k}^N - 2BT_{i,j,k}^N + DT_{i,j+1,k}^N) \quad (2.16)$$

$$U_{zz} = (AT_{i,j,k-1}^N - 2BT_{i,j,k}^N + DT_{i,j,k+1}^N) \quad (2.17)$$

$$T_{i,j,k}^{N+1} = \Delta t (U_{xx} + U_{yy} + U_{zz}) + T_{i,j,k}^N + \frac{\Delta t}{\rho c_p} q_L \quad (2.18)$$

Where:

$T_{i,j,k}^{N+1}$ is the new temperature at node i, j, k [K];

$T_{i,j,k}^N$ is the temperature at node i, j, k at the current time step [K];

α is the thermal diffusivity [$m^2 \cdot s^{-1}$];

κ is the thermal conductivity [$W/m \cdot K$];

Δx etc. is the size of the grid element in the p^{th} direction [m];

and A, B, D are the coefficients in their respective dimension (Eq. (2.14)).

Incorporating B.Cs on the top air exposed face:

$$U_{zz} = \frac{\alpha}{\Delta z^2} \left(\frac{2\Delta z}{\kappa} (-h(T_{i,j,k}^N - T_\infty^N)) - 2T_{i,j,k}^N + 2T_{i,j,k+1}^N \right) \quad (2.19)$$

Equations (2.18) and (2.19) give the full numerical solution to the non-linear heat equation with a convection boundary term and laser heat source. This will allow us to calculate the heat diffusion in the porcine tissue due to laser heating.

As the laser used in the experimental work, operates in a pulsed mode, we account for this in our simulation. We assume that the pulse shape is a triangular pulse, with the peak power, P_{peak} , and pulse length, τ . In the heat simulation we have an additional variable in the term $laserOn(t) \cdot \frac{\alpha \Delta t}{\kappa} q_L$ in Eq. (2.18). This additional variable, $laserOn(t)$, is a boolean value and a function of time, which is defined as:

$$laserOn = \begin{cases} 1, & \text{Laser on} \\ 0, & \text{Laser off.} \end{cases}$$

In the instance where there is more than one pulse, the laser is turned on and off based upon the pulse frequency.

As we are using a simple explicit FDM, the time step is constrained in order to make the solution stable. For a cubic 3D FDM without prescribed flux BCs, yields the constraint: $\Delta t \leq \frac{1}{\delta \alpha}$ where $\delta = \frac{1}{\Delta x^2} + \frac{1}{\Delta y^2} + \frac{1}{\Delta z^2}$. However as we have a convection prescribed boundary condition, the constraint on the time is more severe. Along with this time constraint, the pulse length of the laser also has to be considered. If the time step of the heat simulation is too large it will not

account for the heat deposited by the laser. Thus, the timestep has to be an order of magnitude smaller than the shortest laser pulse.

As the timestep is small, and the grid resolution large, the resultant simulation is slow. Thus the code has been fully parallelised to improve performance. Both the MCRT and heat simulation are independently parallelised. As discussed in Chapter 1, the MCRT simulation is fully parallelised, and the results are passed to the heat simulation.

Parallelisation of the heat simulation is more involved than the ‘embarrassingly parallel’ class of problems that MCRT belongs to. This is due to the heat simulation being dependant on the temperature of adjacent nodes. Thus information will have to be passed from each individual core during computation, as opposed to doing the information passing at the end of the simulation à la MCRT parallelisation. The heat simulation is parallelised using a technique called ‘halo swapping’. This involves splitting up the computational domain (see Fig. 2.6), in this case the tissue medium, and doing the calculations on each domain on a separate core. The ‘halo swapping’ comes in when cores need to communicate with each other about updating their boundary temperature nodes (see Fig. 2.7).

* old data from before nonlinear heat equation * On a workstation computer these simulations were carried out on (Intel Xeon E3-1245 v5, 8 core @ 3.5GHz) led to a speed up of ∼6, over the serial simulation. Using Amdahl’s law [53], the serial portion of the simulation is ∼ 5%, giving a theoretical speed up ∼ 20 times the serial simulation.

After one time step of the heat simulation has been completed, the temperature grid is passed to the tissue damage portion of the simulation to calculate the tissue damage that may have accrued during the heat simulation timestep.

2.2.3 Tissue Damage

2.2.3.1 Introduction

The final portion of the simulation is the tissue damage model. To be able to model damage to the tissue we first need to be able to describe the tissue damage process due to heating from a laser.

When the laser is turned on, the temperature starts to rise within the tissue due to the absorption of photons by the tissue. The temperature rise causes damage to the tissue when above a threshold temperature, T_d , approximately 43°C [54]*p539*. From the temperature, T_d , we define four main areas of tissue damage:

$$T = \begin{cases} \text{coagulation,} & T_d \leq T \leq 100 \text{ } ^\circ\text{C} \\ \text{water boils,} & T = 100 \text{ } ^\circ\text{C} \\ \text{carbonisation,} & 100 \text{ } ^\circ\text{C} \leq T \leq T_a \\ \text{ablation,} & T = T_a. \end{cases} \quad (2.20)$$

The area of tissue damage we term ‘coagulation’ is a multifaceted process. At 43°C - 50°C, bonds break within cell membranes, causing ruptures, and some cell death [54, 55]. This process is usually termed *hyperthermia*. Around 50°C, enzyme activity decreases, cells become immobile, and various cell repair mechanisms are disabled, leading to increased cell death. When temperatures exceed 60°C, proteins become denatured. Thermal denaturation is a structural and functional change in a protein due to the heating it undergoes. This means they change from a highly organised structure with specific purposes, to disorganised structures with little to no function at all. A classic example of denaturation of proteins, is in cooking eggs. Denaturation occurs when the clear fluid egg white, rich in protein albumin, becomes a solid white [56].

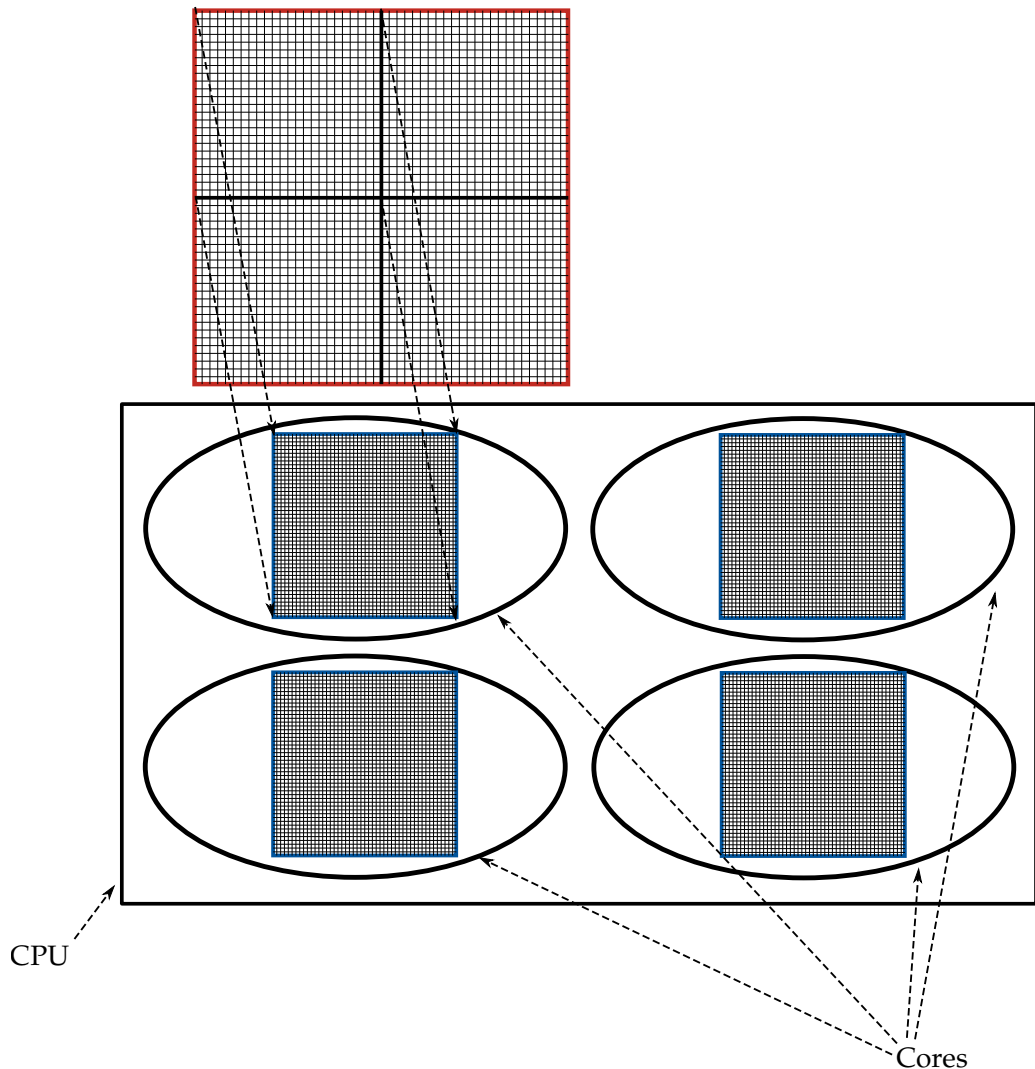


Figure 2.6: Computational domain decomposition. Total computational domain (red outline) is evenly divided between cores in the CPU. This is done via layers of the domain in the z direction. Information is passed to/from cores via the ‘halo swap’ process (see Fig. 2.7).

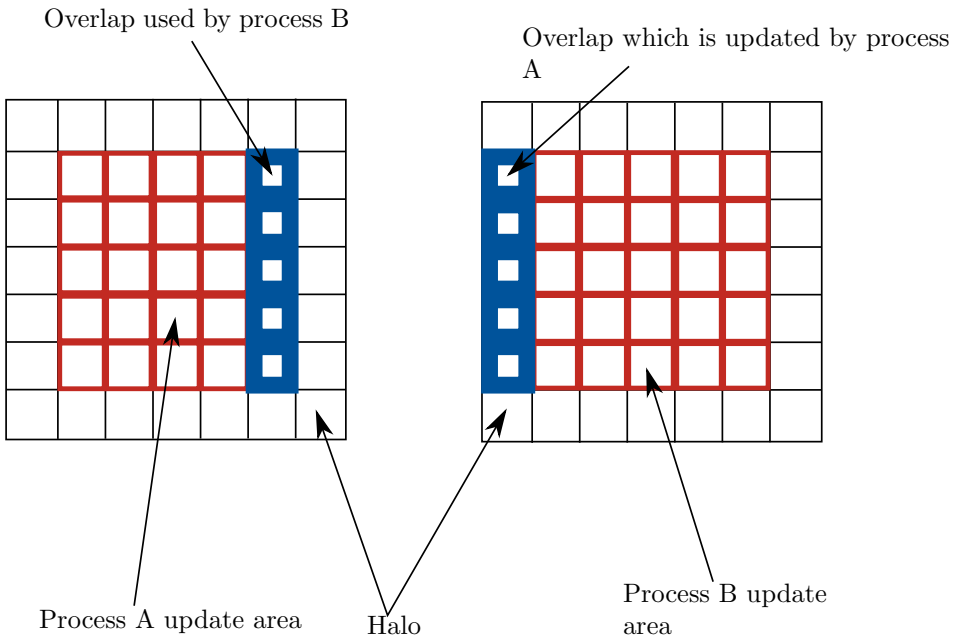


Figure 2.7: Halo swapping. Process A updates the area in red and blue on the left. It updates the blue area which is sent to process B as B's 'halo'. Process B cannot update its own halo, but rather updates the halo for process A.

The next stage in the tissue damage process is the vaporisation of water. As the temperature of the tissue starts to approach 100°C (at 1 atm), water starts to vaporise. If the vaporised water cannot escape the tissue it forms steam vacuoles, small pockets of steam. These vacuoles can easily be seen when viewing tissue samples after tissue has been treated with a high powered laser (see Fig. 2.8). In certain conditions these steam pockets can explode, with these 'explosions' being audible by the human ear [57].

The third stage of tissue damage is carbonisation or caramelisation of the tissue. This occurs when most of the water has boiled off, leaving the remaining tissue to heat up and reduce to its elemental carbon form. This carbonisation of tissue, when it occurs, is generally only a thin layer of 5–20 μm [54, 58].

The final stage of tissue damage is the removal of the remaining tissue, i.e. tissue ablation. There is no agreement in the literature how tissue undergoes ablation with a number of methods proposed [59, 60]. The tissue ablation process is not a simple process, with various unknowns which depend on everything from tissue composition to laser power, wavelength, and pulse length. The literature however, does suggest that it takes place when the tissue temperature is between 177 and 500°C [61–63].

In order to model all these tissue damage processes we split our tissue damage model into two sections: 'physical' damage and coagulation damage. Where 'physical' damage changes the tissue optical and thermal properties, where the coagulation damage has no effect on the tissue's bulk optical or thermal properties.

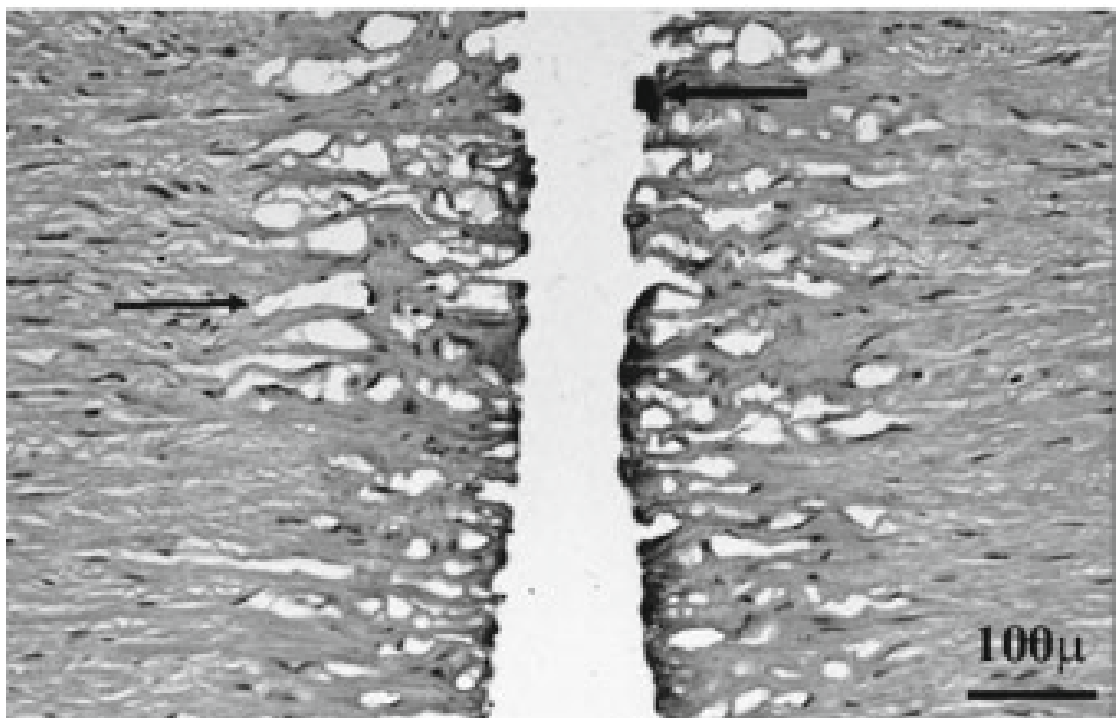


Figure 2.8: Tissue ablations, as viewed under a microscope. Steam vacuoles are clearly visible either side of the ablation area. Carbonisation is also evident at the edges of the ablation fronts. Adapted from [54].

2.2.3.2 Modelling coagulation damage

With the description of the various process that tissue undergoes during ablation, we can now create a numerical model of these processes. First, in order to model the full extent of the damage done under 100°C, i.e in the coagulation regime, we use the Arrhenius damage model. The Arrhenius damage model was originally used as a kinetic model of reaction products in chemistry [64]. It has since been adapted by various authors for modelling tissue damage, and is the *de facto* standard [65, 66]. These authors and various others, adapted this model by fitting Eq. (2.21) to experimental data for burn damage. The two parameters fitted are A, the frequency factor, and ΔE , the activation energy.

$$\Omega(t) = \int_{t_i}^{t_f} Ae^{-\frac{\Delta E}{RT}} d\tau \quad (2.21)$$

Where:

- Ω is the damage value;
- A is ‘frequency factor’ [s^{-1}];
- ΔE is activation energy [$J \cdot mol^{-1}$];
- R is the universal gas constant [$J \cdot mol^{-1} \cdot K^{-1}$];
- T is the temperature [K];
- and t_i and t_f are the initial time and final time at t_{crit} .

It is reported that a value of Ω of 0.53, 1.0, and 10^4 relate to first, second, and third degree burns respectively [67]. We use the Arrhenius damage model in order to better understand the amount of damage caused by the laser in the non-ablated areas of tissue. We adopt of $A = 3.1 \times 10^{98}$, and $\Delta E = 6.27 \times 10^8$ for $T \leq 55$, and for $T > 55$ $A = 5 \times 10^{45}$, and $\Delta E = 2.96 \times 10^8$ [68].

2.2.3.3 Modelling physical tissue damage

As tissue mostly consists of water [69] when the temperature of the tissue approaches 100°C (at 1 atm), water in the tissue begins to boil off. This acts as a large heat sink for the absorbed laser energy, slowing down the rate of ablation. The energy required to boil the water is $Q_{vapor} = m_v \cdot L_v$, where m_v is the mass of a voxel, and L_v is the latent heat of vaporisation. The energy to boil off the water is provided via the laser and heat diffusing into the voxel:

$$Q_{vapor} = \underbrace{laserOn(t) \cdot \dot{q} \cdot \Delta t \cdot V_{i,j,k}}_{\text{laser heating}} + \underbrace{c \cdot M_{i,j,k} \cdot \Delta T}_{\text{heat diffusion}} \quad (2.22)$$

Where:

- Q_{vapor} is the current energy in Joules that has been used to boil off the water in the voxel [J];
- $laserOn$ is a boolean variable that determine if the laser is on or off [-];
- \dot{q} is the energy absorbed by the voxel due to the laser [$W \cdot m^{-3}$];
- Δt is the timestep [s];
- $V_{i,j,k}$ is the volume of the voxel labelled i, j, k [m^3];
- c is the heat capacity of the voxel [$J \cdot K^{-1}$];
- $M_{i,j,k}$ is the mass of the the voxel labelled i, j, k [Kg];
- and ΔT is the change in temperature the voxel would undergo, if the water was not boiling off.

As water boils off, the water content of each voxel changes. This affects the absorption coefficient, density, thermal conductivity, and heat capacity. Each of these vary with water content per voxel [70];

$$W = W_{init} - \left(W_{init} \cdot \left(\frac{Q_{current}}{Q_{vaporisation}} \right) \right) \quad (2.23)$$

$$\rho = \frac{1000}{W + 0.649 \cdot P} \quad (2.24)$$

$$c_p = 4.2 \cdot 10^3 \cdot W + 1.09 \cdot 10^3 \cdot P \quad (2.25)$$

$$\kappa = \rho \cdot (6.28 \cdot 10^{-4} \cdot W + 1.17 \cdot 10^{-4} \cdot P) \quad (2.26)$$

$$\mu_a = W \cdot \mu_{water} + \mu_{protein} \quad (2.27)$$

$$(2.28)$$

Where:

W is the water content (i.e $W = 0.7$ equates to 70% water content);

W_{init} is the initial water content;

$Q_{current}$ is the total energy absorbed by the i^{th} voxel since the temperature reached 100°C [J];

P is the protein content (i.e $P = 1.0 - W$);

κ is the Thermal conductivity [$W \cdot m^{-1} \cdot K^{-1}$];

c_p is the heat capacity [$J \cdot Kg^{-1} \cdot K^{-1}$];

and μ_a is the total absorption coefficient, and μ_{water} and $\mu_{protein}$ are the absorption coefficients of water and protein respectively.

We define the T_a as occurring between 177 and 500°C [61–63]. At T_a the tissue is removed and the thermal, optical, and physical properties set to that of air.

The updated damaged tissue structure is then fed back to the MCRT model and the whole process repeats until the predefined time limit is reached. This whole process of photon propagation, heat diffusion and tissue damage is outlined in Fig. 2.2.

2.2.4 Validation

2.2.4.1 Heat transport validation

In order to thoroughly validate the numerical method we employ to solve the heat equation, we compare the numerical method against an easily solvable analytical case. We solve the heat equation on a cube, side L, in a surrounding medium of 0°C. The cube is initially at temperature 37°C and we calculate the temperature at time $t=0.1s$. Thus the boundary conditions are:

$$T(0, y, z, t) = T(x, 0, z, t) = T(x, y, 0, t) = 0^\circ C \quad (2.29)$$

$$T(L, y, z, t) = T(x, L, z, t) = T(x, y, L, t) = 0^\circ C \quad (2.30)$$

The thermal diffusivity (α), density (ρ), and heat capacity (c_p) are all set to 1. Assuming a separable solution in Cartesian coordinates yields:

$$\begin{aligned} T(x, y, z, t) = & (A_1 \cos(\alpha x) + A_1 \sin(\alpha x)) \cdot \\ & (B_1 \cos(\beta y) + B_1 \sin(\beta y)) \cdot \\ & (C_1 \cos(\gamma z) + C_1 \sin(\gamma z)) \cdot e^{-\alpha \mu^2 t} \end{aligned} \quad (2.31)$$

$$\mu^2 = \alpha^2 + \beta^2 + \gamma^2 \quad (2.32)$$

Applying the boundary conditions (Eqs. (2.29) and (2.30)) gives:

$$A_1 = B_1 = C_1 = 0 \text{ and } \alpha = \frac{\pi n}{L} \quad \beta = \frac{\pi m}{L} \quad \gamma = \frac{\pi p}{L} \quad (2.33)$$

$$\therefore T_{nmp}(x, y, z, t) = A_{nmp} \cdot \sin\left(\frac{\pi n x}{L}\right) \cdot \sin\left(\frac{\pi m y}{L}\right) \cdot \sin\left(\frac{\pi p z}{L}\right) \quad (2.34)$$

This yields the following solution for the heat equation using the principle of superposition, and solving Eq. (2.35) with $f(x, y, z)$ as the initial temperature profile of the cube:

$$A_{nmp} = \frac{8}{L^3} \int_0^L \int_0^L \int_0^L f(x, y, z) \cdot \sin\left(\frac{\pi n x}{L}\right) \cdot \sin\left(\frac{\pi m y}{L}\right) \cdot \sin\left(\frac{\pi p z}{L}\right) dx \cdot dy \cdot dz \quad (2.35)$$

$$T(x, y, z, t) = \sum_{n=1,3,\dots}^{\infty} \sum_{m=1,3,\dots}^{\infty} \sum_{p=1,3,\dots}^{\infty} \frac{2368}{\pi^3 nmp} \cdot \sin\left(\frac{\pi n x}{L}\right) \cdot \sin\left(\frac{\pi m y}{L}\right) \cdot \sin\left(\frac{\pi p z}{L}\right) \cdot e^{(-\lambda^2 t)} \quad (2.36)$$

Where:

$$\lambda^2 = \alpha\pi^2\left(\frac{n^2}{L^2} + \frac{m^2}{L^2} + \frac{p^2}{L^2}\right);$$

n, m, p are odd integers;

and L is the length of the cube.

At time, $t = 0.1\text{s}$, a slice through the middle of the cube, $L = 1\text{ cm}$, yields Fig. 2.9, which shows that the numerical method matches the analytical solution closely.

2.2.4.2 MCRT & heat transport validation

As a first test of our code, both MCRT and heat simulation, we compare to a simple analytical model of ablation. The simple model of ablation is as: We define the ablation energy (E_a) as the minimum energy required to raise the temperature of the medium to $100\text{ }^\circ\text{C}$, and then boil off the water in a volume dV , mass M . Thus in one dimension we have Eq. (2.37), where the symbols have their usual meanings. If the energy for ablation is delivered in a time dt by a laser of power density (W cm^{-2}), P , this gives Eq. (2.38). Equation (2.38) can be rearranged in order to give an ablation front velocity, Eq. (2.39).

$$E_a = c_p \rho dx \Delta T + L_v \rho dx \quad (2.37)$$

$$P \cdot dt = \rho dx (c_p \Delta T + L_v) \quad (2.38)$$

$$u = \frac{P}{\rho(c_p \Delta T + L_v)} \quad (2.39)$$

Assuming the ablation front moves with constant velocity during the ablation, and using $L_v = 2.53 \cdot 10^6\text{ J} \cdot \text{Kg}^{-1}$, $c_p = 4181\text{ J} \cdot \text{Kg}^{-1} \cdot \text{K}^{-1}$ and the medium is a cube side 2 mm , with a starting temperature is $37\text{ }^\circ\text{C}$ with a water content of 70% giving a density of $700\text{ Kg} \cdot \text{m}^{-3}$. For these parameters this gives an ablation velocity, $u \simeq 0.77\text{ cm} \cdot \text{s}^{-1}$, and a time to ablate through 2 mm of tissue of $\simeq 0.26\text{ s}$. As the code developed in this chapter simulates the diffusion of heat in a medium due to an incident laser, the expected time to ablate through the same medium

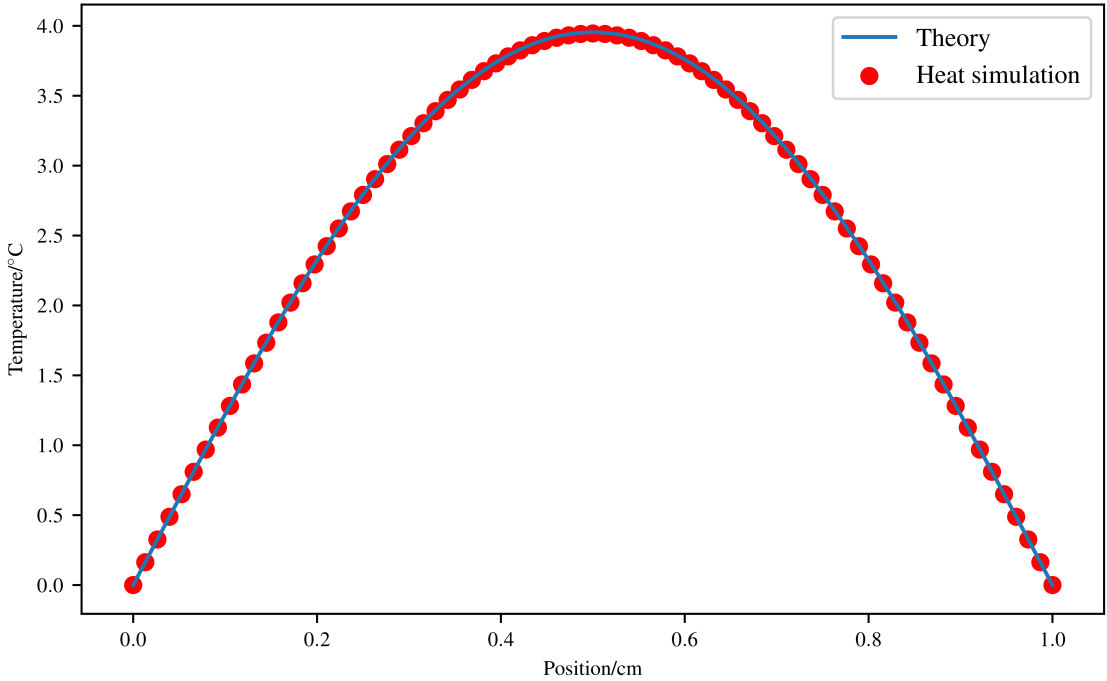


Figure 2.9: Comparison between analytical solution and numerical method at $t=0.1$ s.

should be slightly less as heat diffuses away from the voxel while it is heated being heated. When the full heat + MCRT code is used to simulate this experiment, it gives a time, $t \simeq 0.33$ s.

maybe more? Could compare to <https://doi.org/10.1111/1.2204615>. They use MCRT + FDM but no ablation. So would be good test. Leaving till 2019 if time

2.3 *In silico* results

2.3.1 Introduction

In order to match the experimental results, we must first create as accurate model of the experimental setup *in silico*. However due to computational constraints, such as memory and time available, we must make some approximations to the experimental setup. The porcine skin was a large thin slice of the top most layers of the skin. However as the area of interest is where the ablation occurs, we initially model the porcine skin as a cuboid, dimensions: $1.1 \times 1.1 \times 0.5$ cm. The initial temperature of the porcine skin is assumed to be around 5° , as the tissue was kept on ice or was kept cooled. As mentioned in the previous sections, there are several unknowns in the model: T_a , water content, temperature of air after ablation, and the exact thermal and optical properties of the porcine tissue. Therefore we run several models so that the full parameter space of these unknowns can be explored. Results from these *in silico* experiments are presented in this section along with a comparison of the model to the experimental work carried out in collaboration with the University of Dundee and the Photobiology department at Ninewells hospital.

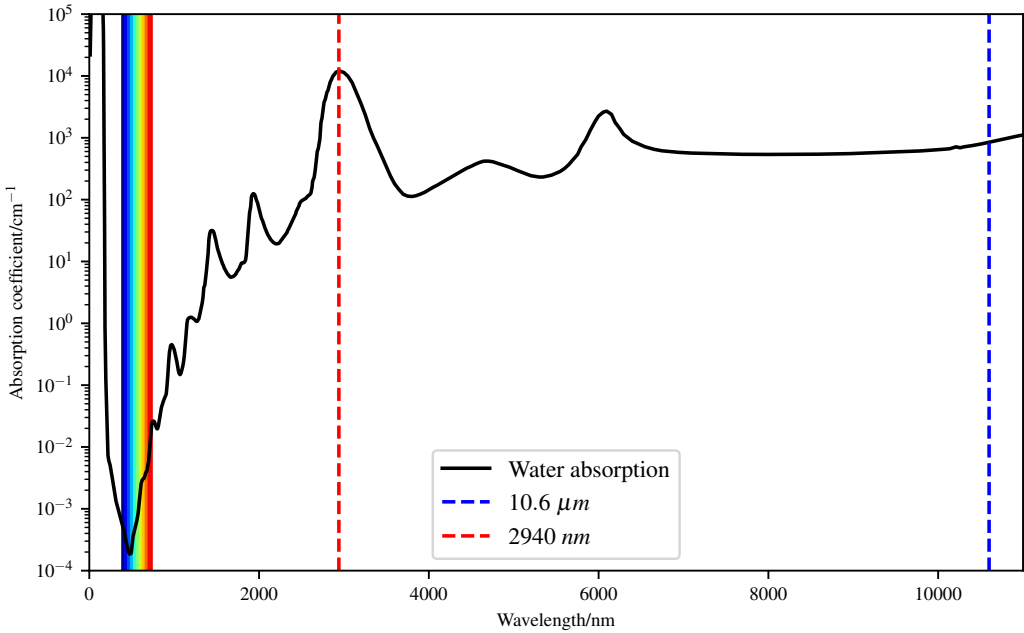


Figure 2.10: Water absorption coefficient for wavelengths 0-12000nm [72]. Data shows that water is highly absorbing in the infra-red portion of the spectrum compared to the visible portion.

	Thermal conductivity, κ	Density, ρ	Heat capacity, c
Tissue	$\rho \cdot (6.28 \cdot 10^{-4} \cdot W + 1.17 \cdot 10^{-4} \cdot P)$	$\frac{1000}{W+0.649 \cdot P}$	$4.2 \cdot 10^3 \cdot W + 1.09 \cdot 10^3 \cdot P$
Air	$ae^{-b(T-273.15)} + c$	$\frac{p_{atm}}{R_{spec}T}$	1006

Table 2.1: Optical and thermal properties for porcine tissue and air.

2.3.1.1 Optical & thermal properties

As mentioned, the thermal and optical properties of porcine tissue are not known exactly for a given tissue sample. This is due to no one tissue sample being exactly the same as another sample, due to various biological factors. As such the thermal and optical properties used in this section are taken from various literature sources.

The laser used in the experimental work is an infrared laser. This means that the optical properties of the tissue are dominated by water absorption (see Fig. 2.10). The laser used in the experiment is the Pixel CO₂ [71]. The Pixel CO₂ laser has a wavelength 10.6 μm which corresponds to an absorption of coefficient of $\sim 850 \text{ cm}^{-1}$. As the absorption coefficient is large, we assume that scattering is negligible at these wavelengths. Table 2.1 summarises the thermal properties for tissue and air used in the simulations.

The laser was used in ‘Pixel beam’ mode. This means that the laser beam is split into an array of smaller beams. The laser used an array 9×9 of 81 pixel beams. The Pixel CO₂ laser was upgraded during the period in which the experimental data was taken, we present both sets of data, pre-upgrade and post-upgrade. The upgrade consisted of an update to the laser power, from $\sim 30 \text{ W}$ to $\sim 70 \text{ W}$.

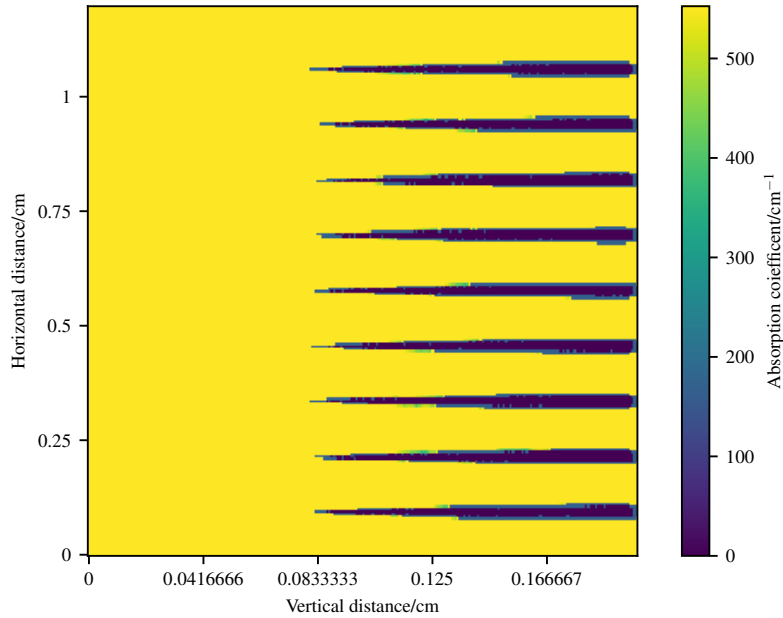


Figure 2.11: Simulation of 81 pixel beams. Figure is a slice through the optical properties at the end of the simulation. Yellow is unchanged tissue, and purple is completely ablated tissue. Figure shows that the ablation craters do not overlap one another.

The laser delivered one single pulse of varying total energy delivered over the range 50 mJ to 400 mJ , in so called “super pulsed mode”. The experiment consisted of ablating the porcine tissue, as a function of energy per ‘pixel’ beam. This was achieved by adjusting the pulse length of the laser, τ , so that the energy per pulse was varied over a range 50 mJ to 400 mJ . The energy range for the laser was kept the same pre and post-upgrade, with the pulse length differing.

2.3.1.2 Computational speed up:

As mentioned in the introduction, the volume of interest is the area around the ablation craters. The volume is $1.1 \times 1.1 \times 0.5 \text{ cm}$. However, in order for the simulation to have good resolution of the ablation craters, this volume would require a large number of voxels for the tissue model. This is infeasible due to: the memory required to store the various counters, grids, and variables, and the time that would be required in order to carry out the computation. Thus the volume of interest is reduced to focus on just one of the ablation craters that is created by the laser. As a sanity check to ensure that we are not omitting any phenomena by focusing on just one ablation crater, an initial simulation that simulates the full volume of interest was carried out to investigate the possibility of overlapping craters or other related phenomena. The simulation, as shown in Fig. 2.11, gives us validation that the shrinking of the volume of interest is a valid approximation to make.

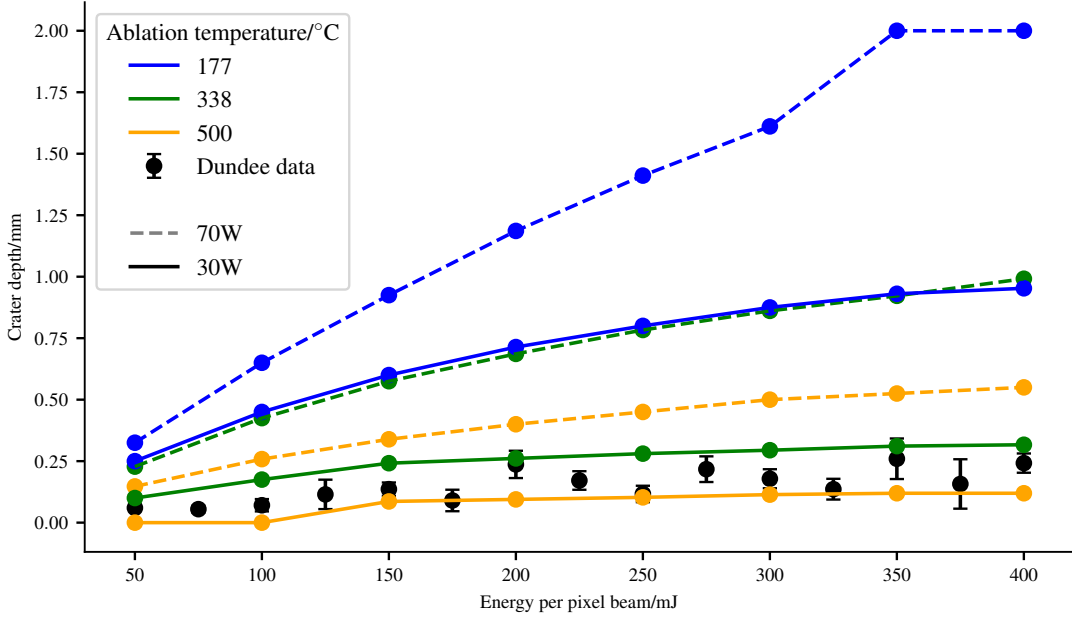


Figure 2.12: Simulations of 30 W and 70 W CO₂ ablative laser. Crater depths as a function of pixel beam energy for various T_a 's. *placeholder until I rerun for triangular pulse.*

2.3.2 Results

2.3.2.1 Investigating ablation temperature, T_a

Various literature sources report the ablation temperature ranging from 177° to 500° [61–63]. Thus, we run several models over this range in order to establish a ‘good’ T_a which fits with the experimental results. Figure 2.12 shows how T_a affects the crater depth as a function of pixel beam energy for the CO₂ laser. Both the 70 W and 30 W simulations agree, that a ‘good’ T_a is around $T_a = tbd$ °C.

Increasing the ablation temperature, has the obvious affect of requiring more energy to be deposited by the laser before ablation takes place. As more energy is required to heat the porcine tissue up to the ablation temperature before it can be ablated. This also allows more heat to diffuse away from the ablation crater increasing the thermal damage done to the surrounding tissue. Decreasing the ablation temperature has the converse affect, and allows the ablation crater to become deeper.

Over the full range of T_a , as the energy per pixel beam increases, there is a trend that at higher energies the crater depth tapers off. This is most likely due to a number of reasons. As the ablation craters grows the volume of tissue that is ablated is replaced with air, allowing more heat loss from the tissue to the environment. As well as heat loss to the environment, more heat is diffused away into the surrounding tissue as the crater grows, due to the availability of more tissue for the heat to diffuse into.

2.3.2.2 Investigating Thermal damage

As stated in Section 2.2.3.2, we use the Arrhenius damage integral in order to estimate the thermal damage due to the laser. In order to calculate the tissue damage around the ablation craters, we first transform Eq. (2.21) in to a summation:

$$\Omega(t) = \int_{t_p}^{t_f} A e^{-\frac{\Delta E}{RT}} d\tau \quad (2.40)$$

$$\Omega(t) = \sum_{m=m_p}^{m_f} A e^{-\frac{\Delta E}{RT_\xi^m}} \Delta t \quad (2.41)$$

Where:

ΔE , R , T , and A have the same meanings as before;

ξ is the i^{th} , j^{th} , k^{th} node;

and m_p is the p^{th} timestep when the ξ^{th} node is above the threshold temperature.

Using Eq. (2.41) we can thus estimate the damage to the tissue on a voxel by voxel basis. Figure 2.13 show how far the thermal damage extends around the ablation crater. For ease of visualisation we map 1-3 to their respective burns via the following scheme, with η as burn severity:

$$\eta = \begin{cases} 3, & \Omega \geq 10000 \\ 2, & 1 \leq \Omega < 10000 \\ 1, & 0.53 \leq \Omega < 1 \\ 0, & 0.0 \leq \Omega < 0.53. \end{cases} \quad (2.42)$$

As evidenced in Fig. 2.13, the thermal damage zone extends for a small distance around the ablation crater, due to the diffusion of heat into these areas.

We can also investigate the time it takes for different areas of the tissue to become thermally damaged. This can be easily achieved by saving the time each voxel passes one of the damage boundaries in Eq. (2.42). Figure 2.16 show the minimum time taken for 1st, 2nd, and 3rd degree burns to occur for both 30 W and 70 W powered lasers as a function of depth. The 70 W laser shows that there is little to no time (upon the order of 0.5 ms) between 1st and 2nd degree burns, and a maximum of ~ 0.02 s between 2nd and 3rd degree burns. The 30 W has a larger time differential between burn classifications, with a maximum of 0.02 s between 1st and 2nd degree burns and a maximum of 0.2 s between 2nd and 3rd degree burns. The spatial distance between burn boundaries are also drastically different between the two different powers of laser. At 70W there is virtually no difference in the boundaries for the 1st and 2nd degree burns, with a slight difference of $\sim 5 \mu m$ between the 2nd and 3rd degree burns. 30 W the distance between 2nd and 3rd is $\sim 11 \mu m$, and for 1st and 2nd $\sim 1 \mu m$.

2.4 Conclusion

Using MCRT and finite difference method, we have created a fully 3D model of photon and heat transport within tissue. This model can be used to simulate the heat deposited by laser, the ablation craters formed via high powered laser and the resultant thermal damage surrounding the ablation crater.

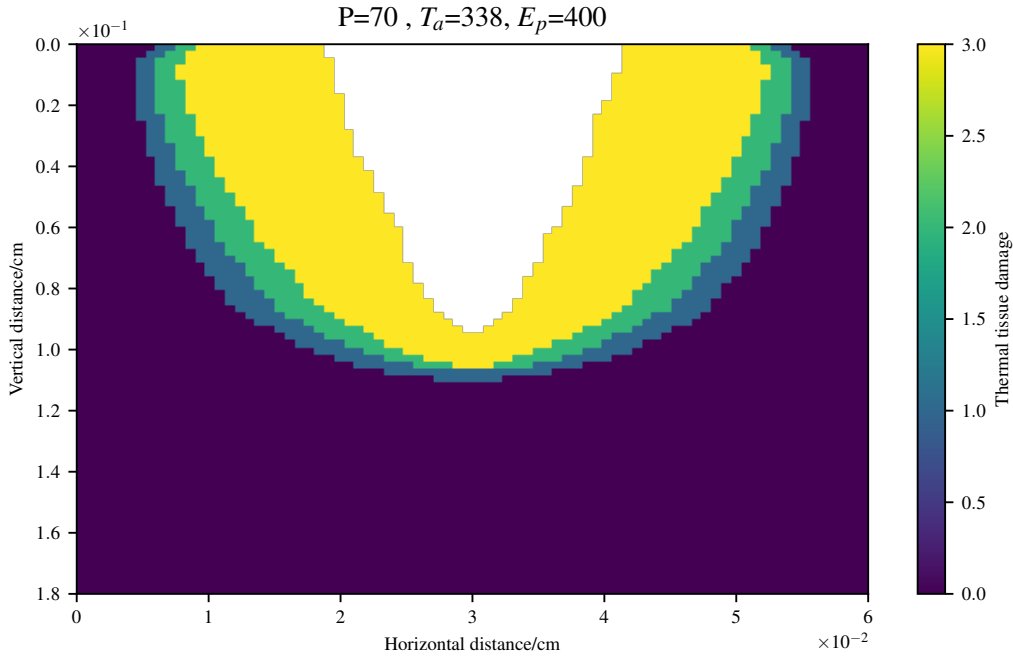


Figure 2.13: Tissue thermal damage around the ablation crater (white). Thermal tissue damage values of 3 refer to 3rd degree burns, 2 to 2nd, and 1 to 1st degree burns respectively. P is the power in Watts, T_a is the ablation temperature in Kelvin, and E_p is the energy per pixel beam in mJ.

Our model has been fully validated against both analytical solutions and experimental results. We found that to match with experimental results that a tissue ablation temperature T_a of around 420 K has to be adopted.

The simulations allow us to predict for a given laser power and pulse length, how much thermal damage is caused in the tissue, and how deep an ablation crater that will form. The computational model could be used in future to help develop treatment regimes for both aesthetic procedures. For example, currently there is a lot of ‘down time’ after skin rejuvenation, in which the patient displays inflammation, erythema, edema, pain, and crusting [73–75]. Simulations of thermal damage due to fractional ablation could help design treatment regimes that minimise these effects, whilst still delivering skin rejuvenation. The model can also be applied to help optimise laser assisted drug delivery. Laser assisted drug delivery consists of using a laser to ‘drill’ holes into the skin in order to help topical medicines diffuse into the skin better, than just applying the medicines to skin with no holes. Our model can help predict the laser parameters needed to reach a certain hole depth, thus minimising thermal damage and pain to patients.

There are many avenues available with regards to future work on this model. The model presented here in this chapter was on a initially homogeneous skin model. In reality skin is compromised of several distinctive layers, with each layer containing varying amounts of different chromophores. Our model can easily incorporate an n -layer skin model complete with various fractions of chromophores. The current model as present is a voxel based model, where all the voxels are the same size. This allows the model presented in this chapter to be easily setup, with regards to parallelisation, optical/thermal properties and ease of programming. However voxel

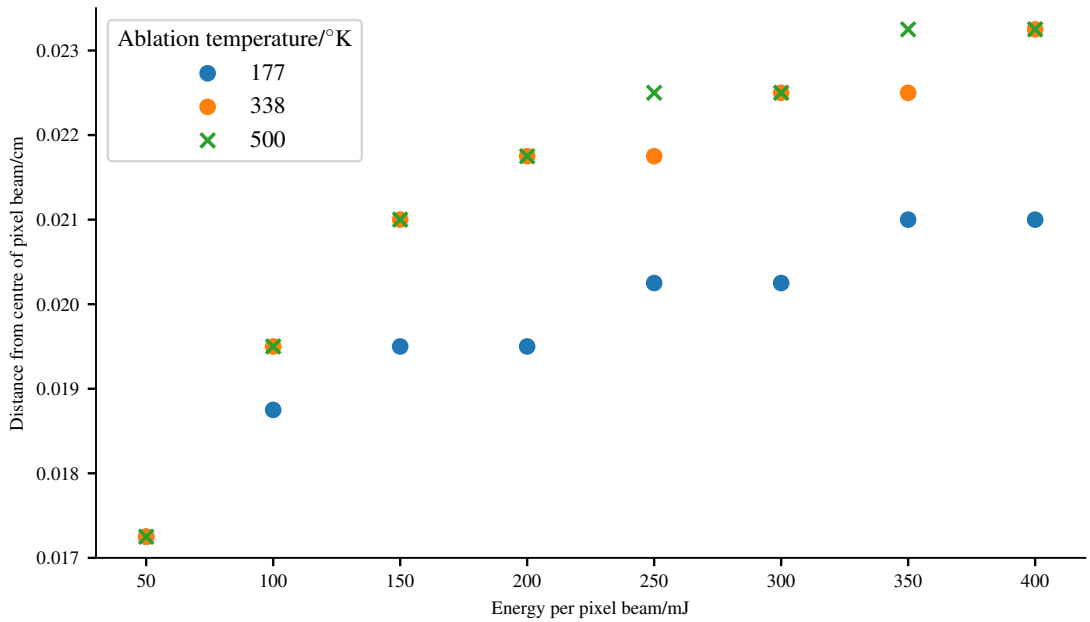


Figure 2.14: Figure shows the maximum horizontal extent of thermal damage as a function of energy per pixel beam for laser of power 30 W.

models, where all the voxels are the same size, are not computationally efficient. Particularly in order to achieve good resolution, many voxels are needed, which requires large amounts of RAM, due to a $\sim n^3$ scaling of voxels to memory in 3D. A more efficient way, would be to allow different sizes of voxels, depending on parts of the model which need high resolution, and parts that do not need high resolution. Such a voxel model is called an [adaptive mesh refinement \(AMR\)](#). There are downsides to [AMR](#): complex implementation for parallelisation and setup of optical/thermal, slower optical depth integration routines due to neighbour lookups.

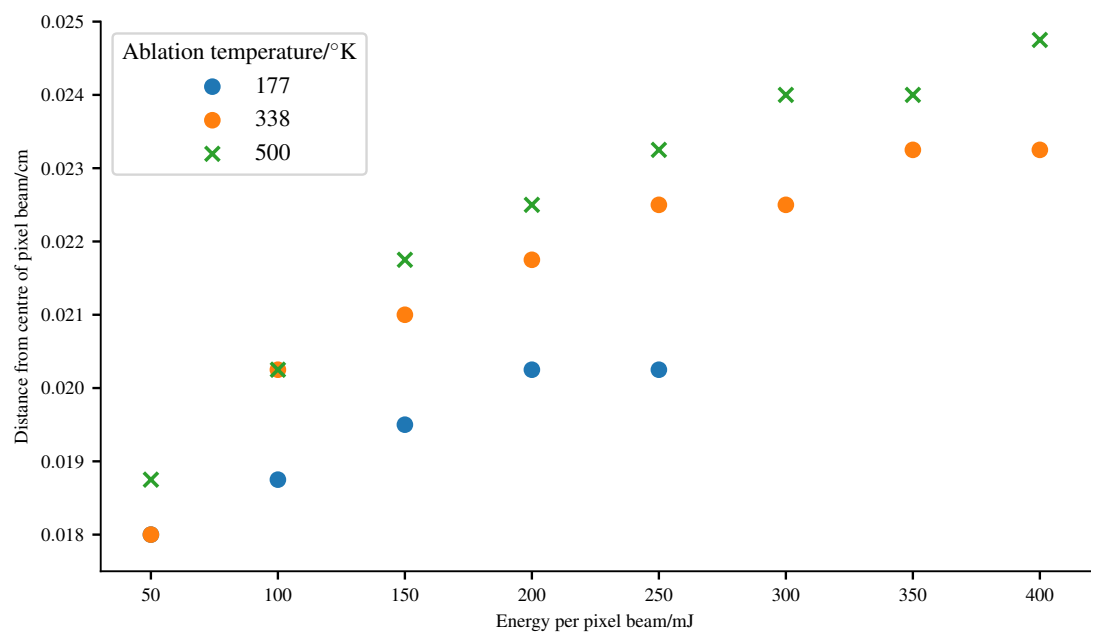


Figure 2.15: Figure shows the maximum horizontal extent of thermal damage as a function of energy per pixel beam for laser of power 70 W.

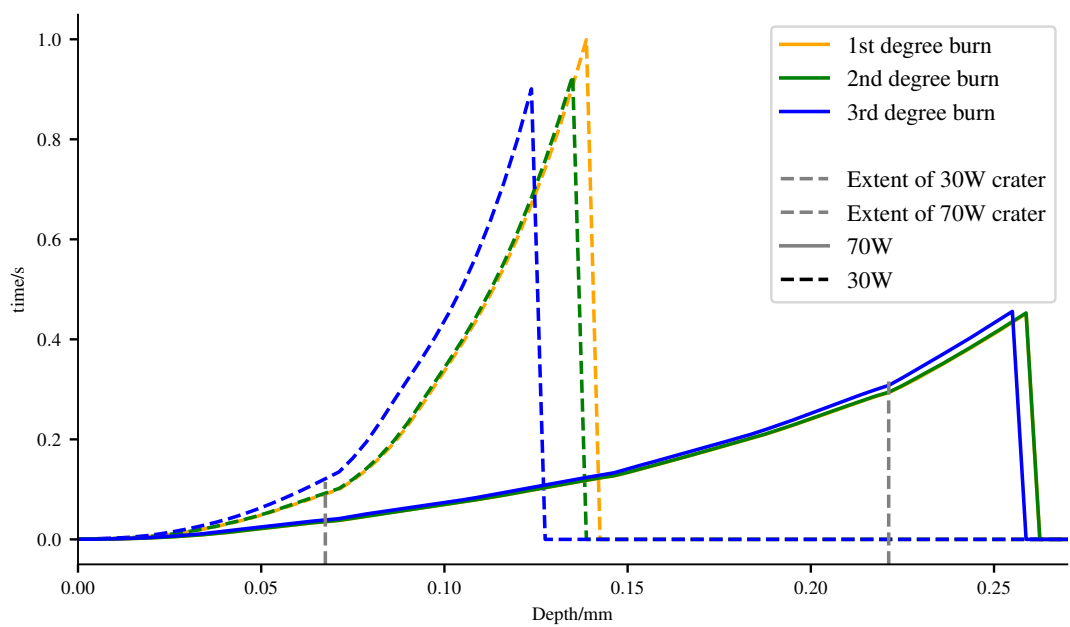


Figure 2.16: Figure shows the extent of burns inflicted by the laser as a function of depth. Lines are taken from the central point of the laser beam through the tissue. Coloured dashed lines are 30W laser and solid coloured lines are 70W laser. Both data sets plotted for ablation temperature of $420\text{ }^{\circ}\text{C}$, and pixel beam energy of 400 mJ

Appendices

Appendix A

Heat equation derivation

To derive the heat equation we consider the conversation of energy in a volume R , with a flux out, $\phi(x, y, z, t)$, and unit outer normal $\hat{\mathbf{n}}$. We need just the normal component of ϕ : $\phi \cdot \hat{\mathbf{n}}$.

The rate of change of heat inside the volume R is equal to the heat generated inside the volume R plus the heat flowing in/out of the boundary surface:

$$\frac{\text{Rate of change of heat energy}}{R} = \frac{\text{Rate of heat generation in}}{R} + \frac{\text{Rate of heat energy flowing through boundary surface}}{R} \quad (\text{A.1})$$

The total heat energy is:

$$e(x, y, z, t) = c(x, y, z) \cdot \rho(x, y, z) \cdot T(x, y, z, t) \quad (\text{A.2})$$

and therefore the rate of change of heat energy is

$$\frac{d}{dt} \iiint_R e \, dV = \frac{d}{dt} \iiint_R c\rho T \, dV \quad (\text{A.3})$$

We denote the heat generated inside the volume R as $Q(x, y, z, t)$:

$$\iiint_R Q \, dV \quad (\text{A.4})$$

and the rate of heat energy flowing through the boundary surface is:

$$-\iint_{\partial R} \phi \cdot \hat{\mathbf{n}} \, dS^{\ddagger} \quad (\text{A.5})$$

Substituting Eqs. (A.3) to (A.5) into Eq. (A.1), yields:

$$\frac{\partial}{\partial t} \iiint_R c\rho T \, dV = -\iiint_R \phi \cdot \hat{\mathbf{n}} \, dV + \iiint_R Q \, dV \quad (\text{A.6})$$

Using the divergence theorem, and simplifying gives:

[†]This is negative as outward flow ϕ is positive, but the flow would result in a reduction of energy.

$$\frac{\partial}{\partial t} \iiint_R c\rho T \, dV = - \iiint_R \nabla \cdot \phi \, dV + \iiint_R Q \, dV \quad (\text{A.7})$$

$$\iiint_R \left[c\rho \frac{\partial}{\partial t} T + \nabla \cdot \phi - Q \right] dV = 0 \quad (\text{A.8})$$

Which holds for an arbitrary R, thus:

$$c\rho \frac{\partial}{\partial t} T = -\nabla \cdot \phi + Q \quad (\text{A.9})$$

Using Fourier's law of heat conduction, which states that the local heat flux density, ϕ , is proportional to the negative local temperature gradient. The proportionality constant being equal to the thermal conductivity, κ :

$$\phi(x, y, z, t) = \kappa(x, y, z) \nabla T(x, y, z, t) \quad (\text{A.10})$$

Substituting Eq. (A.10) into Eq. (A.9) yields the heat equation:

$$c\rho \frac{\partial}{\partial t} T = \nabla \cdot (\kappa \nabla T) + Q \quad (\text{A.11})$$

Which can be simplified into the homogeneous medium heat equation with the following assumptions: $Q=0$ and κ , ρ , and c are constant, and $\alpha = \frac{\kappa}{c\rho}$

$$\frac{\partial T}{\partial t} = \alpha \nabla^2 T \quad (\text{A.12})$$

Bibliography

- [1] Lee Badger. Lazzarini’s lucky approximation of π . *Mathematics Magazine*, 67(2):83–91, 1994.
- [2] Petr Beckmann. *A history of Pi*. St. Martin’s Griffin, 2015.
- [3] Georges-Louis Leclerc Buffon. *Histoire naturelle générale et particulière*, volume 18. de l’Imprimerie de F. Dufart, 1785.
- [4] Peter Jäckel. *Monte Carlo methods in finance*. J. Wiley, 2002.
- [5] David B Hertz. Risk analysis in capital investment. *Harvard Business Review*, 42(1):95–106, 1964.
- [6] Jasper Vivian Wall and Charles R Jenkins. *Practical statistics for astronomers*. Cambridge University Press, 2012.
- [7] James T. Kajiya. The rendering equation. *SIGGRAPH Comput. Graph.*, 20(4):143–150, August 1986.
- [8] Robert L. Cook, Thomas Porter, and Loren Carpenter. Distributed ray tracing. *SIGGRAPH Comput. Graph.*, 18(3):137–145, January 1984.
- [9] Nicholas Metropolis. The beginning of the Monte Carlo method. *Los Alamos Science*, 15:125–130, 1987.
- [10] Roger Eckhardt. Stan Ulam, John von Neumann, and the Monte Carlo method. *Los Alamos Science*, 15:131–136, 1987.
- [11] HL Anderson. Metropolis, Monte Carlo, and the MANIAC. *Los Alamos Science*, 14:96–108, 1986.
- [12] Stanislaw Ulam, RD Richtmyer, and J Von Neumann. Statistical methods in neutron diffusion. *LAMS-551, Los Alamos National Laboratory*, pages 1–22, 1947.
- [13] Kenneth Wood and RJ Reynolds. A model for the scattered light contribution and polarization of the diffuse $h\alpha$ galactic background. *The Astrophysical Journal*, 525(2):799, 1999.
- [14] DWO Rogers, BA Faddegon, GX Ding, C-M Ma, J We, and TR Mackie. Beam: a monte carlo code to simulate radiotherapy treatment units. *Medical physics*, 22(5):503–524, 1995.
- [15] BC Wilson and G Adam. A monte carlo model for the absorption and flux distributions of light in tissue. *Medical Physics*, 10(6):824–830, 1983.

- [16] Lihong V Wang and Hsin-i Wu. *Biomedical optics: principles and imaging*. John Wiley & Sons, 2012.
- [17] Subrahmanyam Chandrasekhar. *Radiative transfer*. Courier Corporation, 2013.
- [18] Vesna Džimbeg-Malčić Željka Barbarić-Mikočević and Katarina Itrić. Kubelka-munk theory in describing optical properties of paper (i). *Technical Gazette*, 18(1):117–124, 2011.
- [19] Marek Jasiński. Modelling of light and human skin interaction using kubelka-munk theory. *Scientific Research of the Institute of Mathematics and Computer Science*, 10(1):71–81, 2011.
- [20] Wai-Fung Cheong, Scott A Prahl, and Ashley J Welch. A review of the optical properties of biological tissues. *IEEE journal of quantum electronics*, 26(12):2166–2185, 1990.
- [21] Macaveiu Gabriela. Mathematical methods in biomedical optics. *ISRN Biomedical Engineering*, 2013, 2013.
- [22] Reindert Graaff, Jan G Aarnoudse, Frits FM de Mul, and Henk W Jentink. Similarity relations for anisotropic scattering in absorbing media. *Optical engineering*, 32(2):244–253, 1993.
- [23] Gilwon Yoon, Scott A Prahl, and Ashley J Welch. Accuracies of the diffusion approximation and its similarity relations for laser irradiated biological media. *Applied Optics*, 28(12):2250–2255, 1989.
- [24] Thomas P Robitaille. On the modified random walk algorithm for monte-carlo radiation transfer. *Astronomy & Astrophysics*, 520:A70, 2010.
- [25] M Min, CP Dullemond, C Dominik, Alex de Koter, and JW Hovenier. Radiative transfer in very optically thick circumstellar disks. *Astronomy & Astrophysics*, 497(1):155–166, 2009.
- [26] Steven L Jacques. Optical properties of biological tissues: a review. *Physics in Medicine & Biology*, 58(11):R37, 2013.
- [27] Steven L Jacques, CA Alter, and Scott A Prahl. Angular dependence of hene laser light scattering by human dermis. *Lasers Life Sci*, 1(4):309–333, 1987.
- [28] Jon E Bjorkman and Kenneth Wood. Radiative equilibrium and temperature correction in monte carlo radiation transfer. *The Astrophysical Journal*, 554(1):615, 2001.
- [29] Thomas P Robitaille. Hyperion: an open-source parallelized three-dimensional dust continuum radiative transfer code. *Astronomy & Astrophysics*, 536:A79, 2011.
- [30] Saeid Amini-Nik, Darren Kraemer, Michael L Cowan, Keith Gunaratne, Puvindran Nadesan, Benjamin A Alman, and RJ Dwayne Miller. Ultrafast mid-ir laser scalpel: protein signals of the fundamental limits to minimally invasive surgery. *PLoS One*, 5(9):e13053, 2010.
- [31] Oon Tian Tan, Karen Sherwood, and Barbara A Gilchrest. Treatment of children with port-wine stains using the flashlamp-pulsed tunable dye laser. *New England journal of medicine*, 320(7):416–421, 1989.
- [32] Marina Kuperman-Beade, Vicki J Levine, and Robin Ashinoff. Laser removal of tattoos. *American journal of clinical dermatology*, 2(1):21–25, 2001.

- [33] Se Hwang Liew. Laser hair removal. *American journal of clinical dermatology*, 3(2):107–115, 2002.
- [34] Christina A Hardaway and E Victor Ross. Nonablative laser skin remodeling. *Dermatologic clinics*, 20(1):97–111, 2002.
- [35] Stanley M Shapshay, M Stuart Strong, Gaspar W Anastasi, and Charles W Vaughan. Removal of rhinophyma with the carbon dioxide laser: a preliminary report. *Archives of Otolaryngology*, 106(5):257–259, 1980.
- [36] Roberto Valcavi, Fabrizio Riganti, Angelo Bertani, Debora Formisano, and Claudio M Pacella. Percutaneous laser ablation of cold benign thyroid nodules: a 3-year follow-up study in 122 patients. *Thyroid*, 20(11):1253–1261, 2010.
- [37] Merete Hædersdal, Fernanda H Sakamoto, William A Farinelli, Apostolos G Doukas, Josh Tam, and R Rox Anderson. Fractional co₂ laser-assisted drug delivery. *Lasers in Surgery and Medicine: The Official Journal of the American Society for Laser Medicine and Surgery*, 42(2):113–122, 2010.
- [38] Macrene R Alexiades-Armenakas, Jeffrey S Dover, and Kenneth A Arndt. The spectrum of laser skin resurfacing: nonablative, fractional, and ablative laser resurfacing. *Journal of the American Academy of Dermatology*, 58(5):719–737, 2008.
- [39] Dieter Manstein, G Scott Herron, R Kehl Sink, Heather Tanner, and R Rox Anderson. Fractional photothermolysis: a new concept for cutaneous remodeling using microscopic patterns of thermal injury. *Lasers in Surgery and Medicine: The Official Journal of the American Society for Laser Medicine and Surgery*, 34(5):426–438, 2004.
- [40] Rong Kong, Martin Ambrose, and Jerome Spanier. Efficient, automated monte carlo methods for radiation transport. *Journal of computational physics*, 227(22):9463–9476, 2008.
- [41] Lihong Wang, Steven L Jacques, and Liqiong Zheng. Mcmlmonte carlo modeling of light transport in multi-layered tissues. *Computer methods and programs in biomedicine*, 47(2):131–146, 1995.
- [42] Gang Yao and Lihong V Wang. Monte carlo simulation of an optical coherence tomography signal in homogeneous turbid media. *Physics in Medicine & Biology*, 44(9):2307, 1999.
- [43] AJ Welch, Craig Gardner, Rebecca Richards-Kortum, Eric Chan, Glen Criswell, Josh Pfefer, and Steve Warren. Propagation of fluorescent light. *Lasers in Surgery and Medicine: The Official Journal of the American Society for Laser Medicine and Surgery*, 21(2):166–178, 1997.
- [44] Catherine Louise Campbell, Kenny Wood, RM Valentine, C Tom A Brown, and H Moseley. Monte carlo modelling of daylight activated photodynamic therapy. *Physics in Medicine & Biology*, 60(10):4059, 2015.
- [45] David A Boas, JP Culver, JJ Stott, and AK Dunn. Three dimensional monte carlo code for photon migration through complex heterogeneous media including the adult human head. *Optics express*, 10(3):159–170, 2002.
- [46] Sachin V Patwardhan, Atam P Dhawan, and Patricia A Relue. Monte carlo simulation of light-tissue interaction: three-dimensional simulation for trans-illumination-based imaging of skin lesions. *IEEE transactions on biomedical engineering*, 52(7):1227–1236, 2005.

- [47] Kenneth Wood, LM Haffner, RJ Reynolds, John S Mathis, and Greg Madsen. Estimating the porosity of the interstellar medium from three-dimensional photoionization modeling of h ii regions. *The Astrophysical Journal*, 633(1):295, 2005.
- [48] Isla Rose Mary Barnard, Patrick Tierney, Catherine Louise Campbell, Lewis McMillan, Harry Moseley, Ewan Eadie, Christian Tom Alcuin Brown, and Kenneth Wood. Quantifying direct dna damage in the basal layer of skin exposed to uv radiation from sunbeds. *Photochemistry and photobiology*.
- [49] Boris Majaron and Matija Milanič. Effective infrared absorption coefficient for photothermal radiometric measurements in biological tissues. *Physics in Medicine & Biology*, 53(1):255, 2007.
- [50] LB Lucy. Computing radiative equilibria with monte carlo techniques. *Astronomy and Astrophysics*, 344:282–288, 1999.
- [51] David Vernon Widder. *The heat equation*, volume 67. Academic Press, 1976.
- [52] Necati Ozisik. *Finite difference methods in heat transfer*. CRC press, 1994.
- [53] Gene M Amdahl. Validity of the single processor approach to achieving large scale computing capabilities. In *Proceedings of the April 18-20, 1967, spring joint computer conference*, pages 483–485. ACM, 1967.
- [54] Ashley J Welch, Martin JC Van Gemert, et al. *Optical-thermal response of laser-irradiated tissue*, volume 2. Springer, 2011.
- [55] Neil T Wright. Quantitative models of thermal damage to cells and tissues. In *Heat Transfer and Fluid Flow in Biological Processes*, pages 59–76. Elsevier, 2015.
- [56] Markolf H Niemz. *Laser-tissue interactions: fundamentals and applications*. Springer Science & Business Media, 2013.
- [57] Francesco Petrella, Sergio Cavalieri, and Lorenzo Spaggiari. Popcorn effect. *Journal of bronchology & interventional pulmonology*, 20(2):193–194, 2013.
- [58] RM Verdaasdonk, C Borst, and MJC Van Gemert. Explosive onset of continuous wave laser tissue ablation. *Physics in Medicine & Biology*, 35(8):1129, 1990.
- [59] Alfred Vogel and Vasan Venugopalan. Mechanisms of pulsed laser ablation of biological tissues. *Chemical reviews*, 103(2):577–644, 2003.
- [60] AL McKenzie. Physics of thermal processes in laser-tissue interaction. *Physics in Medicine & Biology*, 35(9):1175, 1990.
- [61] Miron Gerstmann, Y Linenberg, Abraham Katzir, and Solange Akselrod. Char formation in tissue irradiated with a CO₂ laser: model and simulations. *Optical Engineering*, 33(7):2343–2352, 1994.
- [62] Alan L McKenzie. A three-zone model of soft-tissue damage by a CO₂ laser. *Physics in Medicine & Biology*, 31(9):967, 1986.
- [63] Aharon Sagi, Ariella Avidor-Zehavi, Avraham Shitzer, Miron Gerstmann, Solange Akselrod, and A Katzir. Heating of biological tissue by laser irradiation: temperature distribution during laser ablation. *Opt. Eng.*, 31(7):1425–1431, 1992.

- [64] John A Pearce. Relationship between arrhenius models of thermal damage and the cem 43 thermal dose. In *Energy-based Treatment of Tissue and Assessment V*, volume 7181, page 718104. International Society for Optics and Photonics, 2009.
- [65] FC Jr Hendriques. Studies of thermal injury; the predictability and the significance of thermally induced rate processes leading to irreversible epidermal injury. *Arch. Pathol. (Chic)*, 43:489–502, 1947.
- [66] SC Jiang, N Ma, HJ Li, and XX Zhang. Effects of thermal properties and geometrical dimensions on skin burn injuries. *Burns*, 28(8):713–717, 2002.
- [67] KR Diller and LJ Hayes. A finite element model of burn injury in blood-perfused skin. *Journal of biomechanical engineering*, 105(3):300–307, 1983.
- [68] Hanglin Ye and Suvranu De. Thermal injury of skin and subcutaneous tissues: A review of experimental approaches and numerical models. *Burns*, 43(5):909–932, 2017.
- [69] Igor V Meglinski and Stephen J Matcher. Quantitative assessment of skin layers absorption and skin reflectance spectra simulation in the visible and near-infrared spectral regions. *Physiological measurement*, 23(4):741, 2002.
- [70] Bruna R Loiola, Helcio RB Orlande, and George S Dulikravich. Thermal damage during ablation of biological tissues. *Numerical Heat Transfer, Part A: Applications*, pages 1–17, 2018.
- [71] Alma Lasers. Pixel CO₂, 2018.
- [72] David J Segelstein. *The complex refractive index of water*. PhD thesis, University of Missouri-Kansas City, 1981.
- [73] Moshe Lapidoth, Shlomit Halachmi, Sarit Cohen, and Dan Ben Amitai. Fractional co2 laser in the treatment of facial scars in children. *Lasers in medical science*, 29(2):855–857, 2014.
- [74] Mario A Trelles, Michael Shohat, and Fernando Urdiales. Safe and effective one-session fractional skin resurfacing using a carbon dioxide laser device in super-pulse mode: a clinical and histologic study. *Aesthetic plastic surgery*, 35(1):31–42, 2011.
- [75] Elisabeth Kohl, Julia Meierhöfer, Michael Koller, Florian Zeman, Leopold Groesser, Sigrid Karrer, Ulrich Hohenleutner, Michael Landthaler, and Silvia Hohenleutner. Fractional carbon dioxide laser resurfacing of rhytides and photoaged skin—a prospective clinical study on patient expectation and satisfaction. *Lasers in surgery and medicine*, 47(2):111–119, 2015.